Aggregation Dynamics: Numerical Approximations, Inverse Problems, and Generalized Sensitivity

by

Dustin D. Keck

B.S. in Aerospace Engineering, North Carolina State University, 1997

M.S. in Applied Mathematics, University of Colorado-Colorado Springs, 2008

A thesis submitted to the
Faculty of the Graduate School of the
University of Colorado in partial fulfillment
of the requirements for the degree of
Doctor of Philosophy
Department of Applied Mathematics
2014

This thesis entitled:
Aggregation Dynamics: Numerical Approximations, Inverse Problems, and Generalized Sensitivity
written by Dustin D. Keck
has been approved for the Department of Applied Mathematics

Prof. David M. Bortz (chair)

Prof. Vanja Dukic

Prof. Keith Julien

Prof. Juan Restrepo

Prof. John Younger

Date ____________________

The final copy of this thesis has been examined by the signatories, and we find that both the content and the form meet acceptable presentation standards of scholarly work in the above mentioned discipline.

Keck, Dustin D. (Ph.D., Applied Mathematics)

Aggregation Dynamics: Numerical Approximations, Inverse Problems, and Generalized Sensitivity

Thesis directed by Prof. David M. Bortz

In this dissertation, we investigate several important mathematical and computational issues that arise when using the Smoluchowski coagulation equation as a model for bacterial aggregation. In particular, we study the accuracy and robustness of numerical simulations and their impact upon related inverse problems. We also study how generalized sensitivity enhances experimental design optimization with an ultimate goal of comparing with experimental data.

First, we study the impact of discretization strategy on the accuracy of solution moment. We perform this investigation in anticipation of comparing with different distributions moments reported by specific experimental devices. For multiplicative aggregation kernels, finite volume methods are superior to finite element methods both in accuracy and computational effort. Conversely, for slowly aggregating systems the finite element approach can produce as little error as the finite volume approach and achieves more accuracy approximating the zeroth moment (at a substantially reduced computational cost).

A better understanding of bacterial aggregation dynamics could also lead to improvements in the treatment of bacterially mediated, life-threatening human illnesses. Therefore, to reach towards our ultimate goal, we examine the inverse problem of estimating the aggregation rate from experimental data. In this study, we develop a methodology for a software implementation of parameter fitting when solving inverse problems involving the Smoluchowski coagulation equation. Additionally, we make the novel extension of generalized sensitivity functions (GSFs) for ordinary differential equations to GSFs for partial differential equations. We analyze the GSFs in the context of size-structured population models, and specifically analyze the Smoluchowski coagulation equation in order to determine the most relevant time and volume domains for three, distinct aggregation kernels. Finally, we provide evidence that parameter estimation for the Smoluchowski coagulation equation does not require post-gelation data.

Dedication

I dedicate this dissertation to my wife, Regan, who inspires me every single day, and to my late Uncle Foob, who never let us forget, 'Homer loves beer.'

Acknowledgements

First and foremost, I thank my advisor, Dr. David Bortz, for all of his support, guidance, and mentoring, without which I could never have reached my goals. I also thank my family for providing me the confidence to pursue my dreams and the grounding I have needed to keep me from drifting aimlessly. I owe a deep debt of gratitude to Colonel John Andrew and the United States Air Force Academy Department of Mathematical Sciences for providing me this opportunity. I cannot wait to begin repaying that debt. To my friend, Toby Jones, thank you, thank you, thank you. Time is our most precious resource, and you generously lent me an exceptional amount of your own. I would not be writing this document without your help. Finally, I thank the members of my committee for their time and support.

The views expressed in this dissertation are those of the author and do not reflect the official policy or position of the United States Air Force, Department of Defense, or the U.S. Government.

Contents

Chapter

Appendix

List of Tables

Table

List of Figures

Figure

Chapter 1

Introduction

In this dissertation, we investigate the Smoluchowski coagulation equation, an important size structured population model for describing biological aggregation. For our purposes, aggregation refers to the clustering of particles or groups of particles to form larger clusters. It forms one component of flocculation, which is the process whereby clusters of particles aggregate and fragment while in a fluid. Throughout this paper we use **coagulation**, **aggregation**, and **clustering** interchangeably, as is convention in much of the literature.

We are specifically interested in the aggregation dynamics of the human bacterial pathogen, **Klebsiella pneumoniae**, which can cause pneumonia and other infections. A better understanding of the **Klebsiella pneumoniae** aggregation dynamics could lead to improvements in the treatment of bacterially mediated, life-threatening human illnesses.

The Smoluchowski coagulation equation was originally developed by Marian von Smoluchowski in the early 1900's [86,87] to study gelling colloids. More recently, researchers have employed variations of this model to study organic phenomena such as bacterial growth [20], marine snow [48], algal blooms [1,2,79], sediment transport in tidal cycles [63], and schooling fish [72] and inorganic phenomena such as powder metallurgy [51], astronomy [56,57,65,81], aerosols [34], irradiation of metals [83], electrorheology [69],and meteorology [76]. Furthermore, because only a few known analytic solutions exist, numerical solutions to the Smoluchowski coagulation equation play an important role in the study of this equation [57]. A number of computational approaches have been formulated using finite elements [20,64], finite volumes [43,88], successive approximations [77], method of moments [15,62], Monte Carlo simulations [49,60], and mesh-free approaches that capitalize on radial basis functions [78]. For more comprehensive treatments of the numerics involved with the Smoluchowski coagulation equation, we direct the interested reader to empirical comparisons of numerical techniques by Lee [57] and more recently by Bordás et al. [19].

The following overview provides a brief summary of some important works in the field. Aldous [5] provides an excellent survey (up to its respective date of publishing) concerning mathematical properties of solutions to the Smoluchowski coagulation equation. In [46], Fournier and Laurençot provide a major advancement by proving uniqueness of measure-valued solutions assuming only a finite moment corresponding to the degree of homogeneity of the aggregation kernel. Their work can be viewed as complementary to that of Norris in [73], which does not require any regularity of the aggregation kernel, but does require more of the initial conditions.

The inverse problem of parameter estimation associated with the Smoluchowski equation has garnered significant attention. In [3], Ackleh, Fitzpatrick, and Hallam prove convergence of spline-based collocation methods for approximating the Smoluchowski coagulation equation. Then citing theory regarding minimization of a least squares formulation of the parameter estimation problem (developed by Banks and Kunisch in [14]), the authors further prove existence and stability of solutions to the inverse problem. Ackleh, Hallam, and Muller-Landaus subsequently [4] apply the approach from [3] to data from the 1993 SIGMA tank experiment at Santa Barbara for modeling aggregation and a phytoplankton growth.

First in a series of similar studies of the inverse problem that focus on estimation of the fragmentation parameter, Perthame and Zubelli introduce an atypical regularization method to a specific cell-division model which assumes equal mitosis [75]. Their approach draws on earlier work from [68], [74], and [67], which allows reformulation of the model into an eigenproblem through General Relative Entropy. Then in [31], Doumic, Perthame, and Zubelli expand that work by offering an alternate regularization method and provide numerical experiments confirming their theoretical estimates of convergence rates. Doumic and Gabriel [33] subsequently expand the analysis of the eigenproblem. This expansion of the eigenproblem incorporates more general growth rates than previously studied in [28] and [67] and allows a broader study of asymptotic behavior of solutions. Doumic's, Pedro Maia's, and Jorge P. Zubelli's work in [30] test the eigenproblem reformulation on experimental cell volume distributions of **E. coli** reported in available literature. In [32], to further expand the ideas in [75], [31], and [33], Doumic and Tine provide the same types of results but with general growth rates and with a more general birth rate that allows daughter flocs of unequal sizes. Additionally, the authors in [29] tackle the same problem discussed in [75], [31], and [33] but take a statistical approach. The result of their simulations reproduce global behavior accurately, but do not capture finer details and cannot recover the division rate for large cell volumes.

Another group of studies broaden results for the Smoluchowski coagulation equation to the coagulation-fragmentation equations. In [8] and [7], Ball, Carr, and Penrose pioneer the efforts to prove existence and uniqueness of solutions of the discrete coagulation-fragmentation (DCF) equations under various assumptions on the initial data as well as the coagulation and fragmentation kernels. Then da Costa [25] advances those results by making the assumption of strong fragmentation. In [41], the authors initially only consider situations where gelation, which we define later in this work, occurs in the continuous coagulation-fragmentation (CCF) equations, and they extend functional analysis of weak solutions to the Smoluchowski coagulation equation to the broader CCF equations. The authors provide provide proofs (similar in nature to those of Laurençot in [52]) of existence of weak solutions to the CCF and proofs of gelation under strong fragmentation assumptions and under the assumption of detailed balance. Then in [40], Escobedo et al. fill in the gaps of [41] by adapting a proof from [90] in which Wennberg proves a similar result for the Boltzmann equation. Additionally, Escobedo, Mischler, and Rodriguez Ricard prove in [42] the existence of a stationary solution of any given mass to the CCF equation without assuming a detailed balance condition. As another important advancement in the study of the CCF equations, Laurençot and Mischler make a formal link between solutions of the DCF and CCF equations in [54]. Then by establishing an H-Theorem[1] in [55], Laurençot and Mischler provide proof of convergence to equilibrium for the CCF equations, which mirrors a proof by Lu [61] for the Boltzmann equation. Additionally, Laurençot creates a bridge in [53] between the Smoluchowski coagulation equation and the Oort-Hulst-Safronov (OHS) coagulation equation by making similar arguments to prove existence of solutions with a multiplicative kernel in the latter. Most recently, Giri, Laurençot, and Warnecke [50] provide a proof of existence of weak solutions to the CCF equation with **multiple fragmentation**, which means a single cluster can fragment into more than two daughter flocs. Prior to their study, the vast majority of the research on the CCF equations included only binary fragmentation.

To our knowledge, an as of yet unexplored area regarding the Smoluchowski coagulation equation

---

[1] An H-theorem refers to the increase in entropy of irreversible processes.

lies in a general sensitivity analysis. Generalized sensitivity offers the potential for enhancing experimental design, but previous to our work, researches have only applied it to ordinary differential equations (ODEs) [9–11, 17, 84]. This motivated our even broader work of extending previous developments of generalized sensitivity functions to a partial differential equation (PDE) context.

Before proceeding, we note that while a mean-field approach to modeling particles in suspension can be very useful, we must use care with our terminology. Throughout this paper, we refer to two types of **distributions** over a particle volume domain of interest, $\mathbf{X} \subset \mathbb{R}_+$. In both cases, we use distribution in the sense that we identify a quantity of aggregates per total volume of the aggregates in $\mathbf{X}$. First we denote a **size distribution** $f = f(t, x) \geq 0$ as the **number** density of aggregates of a given volume x at time $t \geq 0$. We denote a **volume distribution** $g = g(t, x)$ as the **volume** density of aggregates of a given volume x. A superscript N_x will denote numerical approximation, e.g., f^{N_x}, g^{N_x}**, etc**. Note that the volume distribution relates to the size distribution as $g(t, x) = xf(t, x)$.

To further promote clarity, we define the **partial i^{th} moment** as

$$M_i(f(t,\cdot); x_1, x_2) = \int_{x_1}^{x_2} x^i f(t,x)dx \tag{1.1}$$

where $f(t, \cdot)$ is the size distribution at time t. For example, $M_0(f(t,\cdot); x_1, x_2)$ or $M_0(\frac{g(t,\cdot)}{(\cdot)}; x_1, x_2)$ represents the total number of clusters having volumes between x_1 and x_2, and $M_1(f(t,\cdot); x_1, x_2)$ or $M_1(\frac{g(t,\cdot)}{(\cdot)}; x_1, x_2)$ represents the total volume of clusters where each cluster included in the total volume individually has a volume between x_1 and x_2.

When using models derived from the Smoluchowski equation to study the real world, we aim to compare a simulated solution to experimental data with the eventual goal to illuminate some scientific phenomenon. Naturally, different experiments yield different types of data, just as different discretization schemes yield varying accuracies for the approximations of different quantities. Accordingly, the type of data should guide the choice of numerical scheme. For example, experimentalists utilizing a Coulter counter [92] often provide data in the form of a vector of partial zeroth moments. Conversely, when employing a flow cytometer [80] or dynamic light scattering instrumentation [18], data is often reported as a partial first moment. Therefore it is important to choose a discretization scheme based on which moment is reported by the specific experimental apparatus. Furthermore, determining an optimum experimental domain from which we gather data reduces expense and improves experimental design. Finally, no experimental device will provide full information about the whole positive real axis; there will always be limited ranges for reliable data. Accordingly, we must also address the additional issue of how to deal with a lack of information about particle aggregates outside the detection limits of a given device.

Therefore, with data considerations as our guide, in Chapter 2, we compare two numerical schemes that provide solutions to the Smoluchowski equation. Then in Chapter 3, we summarize well-posedness of the inverse problem of determining the aggregation kernel from experimental data and provide robustness results for our parameter estimation procedure. Finally, in Chapter 4, we extend to a PDE context the concepts of generalized sensitivity functions that had only previously been applied to ODEs. Additionally, we provide a case study of our extension as it relates to the Smoluchowski coagulation equation for determining an optimal experimental data domain.

Chapter 2

Numerical Simulation of Solutions and Moments of the Smoluchowski Coagulation Equation

In this chapter, we consider a **Finite Element Method** (**FEM**) approach developed in Banks and Kappel [13] (extended by Ackleh and Fitzpatrick [2], and explored in Bortz et al. [20]). We also consider a finite volume-type scheme, which we designate as the **Filbet and Laurençot Flux Method** (**FLFM**), developed in [43].

For both discretization approaches, we pay particular attention to the aggregate volume domain $\mathbf{X}$ and its limits. With both discretizations of $\mathbf{X}$, we lose information, and the impact of that loss on the respective method's accuracies deserves investigation. In that light, a goal of this work is to fully compare the two schemes in terms of their accuracy in approximating a solution and their accuracy in approximating zeroth and first moments and in terms of computation cost. Our numerical investigation supports second order convergence of both methods to fine grid solutions and to the zeroth and first moments.[1] Additionally, our investigation reveals that when modeling slowly aggregating systems, the FEM can provide as little error approximating a true solution as the FLFM and more accurately approximates the zeroth moment, but does so with significantly less computation cost. Conversely, the FLFM approximates the zeroth moment slightly more accurately for slowly aggregating systems, and approximates the first moment more accurately in general.

This chapter is organized as follows. Section 2.1 describes each of the two methods. Section 2.2 provides a description of the explicit solutions studied. Section 2.3 discusses the results of our numerical computations, and Section 4.4 summarizes the results of this chapter.

---

[1] Note that it is commonly reported in the literature that the FEM is only first-order convergent. See Section 2.1.2 for a discussion.

2.1 Numerical Methods

Of the multiple numerical schemes mentioned in the introduction, we restrict ourselves to the FEM originally developed in Banks and Kappel [13] and extended by Ackleh and Fitzpatrick [2] and the FLFM described by Filbet and Laurençot in [43]. In Section 2.1.1, we give a brief description of the Smoluchowski coagulation equation and the common assumptions both methods use in numerically solving the equation. In Section 2.1.2, we highlight the most important parts of the FEM model and the aggregation vectors it creates. Then in Section 2.1.3, we do the same for the FLFM model.

2.1.1 Model and Discretization Overview

In the early 1900's, van Smoluchowski developed a model to study the coagulation of colloids,

$$\frac{d}{dt}f_k = \frac{1}{2}\sum_{i+j=k} K(i,j)f_i f_j - \sum_{i} K(i,k)f_i f_k, \tag{2.1}$$

where f_k represents the number density of aggregates of volume k, and $K(i,j)$ is the aggregation kernel denoting the rate at which aggregates of size i and j form a combined aggregate of size $i+j$ [20, 86, 87]. Müller subsequently extended this model to a continuous PDE [43, 70]

$$\begin{aligned} \partial_t f &= A(f),\ (t,x) \in \mathbb{R}_+^2, \qquad (2.2)\\ f(0) &= f_0,\ x \in \mathbb{R}_+ \end{aligned}$$

where we describe each aggregate solely by its volume $x > 0$, with $f = f(t,\cdot)$ representing the continuous size distribution function of aggregates at time $t \geq 0$. The coagulation term is

$$\begin{aligned} A(f) &= A_{in}(f) - A_{out}(f)\\ &= \frac{1}{2}\int_0^x K(y,x-y)f(t,y)f(t,x-y)dy - f(x)\int_0^\infty K(x,y)f(y)dy \qquad (2.3) \end{aligned}$$

where $K(x,y)$ is the aggregation kernel indicating the rate at which aggregates of volumes x and y join together creating an aggregate of volume $x+y$. Notice the first integral, $A_{in}(f)$, describes aggregates with volumes y and $x-y$ aggregating to a combined volume x, and the second integral, $A_{out}(f)$, models interactions between the aggregate of volume x with all other aggregates of volume y forming an aggregate of volume $x+y$. Also, note that the aggregation kernel $K(x,y)$ is positive and symmetric

$$0 < K(x,y) = K(y,x),\ (x,y) \in \mathbb{R}_+^2,$$

as well as homogeneous, which literature in this field defines as

$$K(\lambda x, \lambda y) = \lambda^m K(x,y),\ \ \lambda > 0,\ m \geq 0,\ x, y < \infty. \tag{2.4}$$

Because only aggregation is considered, the total number of particles decreases with each coagulation event.

The conservation properties of the model in (2.3) warrant a brief discussion. The model is based on conservation of mass principles, but practically speaking, in our simulations, we expect to **lose** mass from the system. First, for aggregation kernels such as the multiplicative kernel, $K(x,y) = xy$, the system experiences growth rapid enough that aggregates with **infinite** volume develop in finite time [89]. This phenomenon is commonly referred to as **gelation**. Mass is not physically lost, but the aggregates with **infinite** volume possess fundamentally different mathematical properties than the individual aggregates that make up the gel. We direct the interested reader to [93], in which Ziff and Stell provide a thorough description of the implications of various assumptions on the post-gelation behavior of the solutions and of the moments. Second, when we discretize the equation, the domain will naturally have a finite maximum value, $\overline{x}$, replacing the infinite upper integration limit of the second integral in (2.3). Therefore, the approximate solution will not include any impact of aggregates larger than $\overline{x}$.

In this chapter, we consider two aggregation kernels, the identity kernel, $K(x,y) \equiv 1$, and the multiplicative kernel, $K(x,y) = xy$ (both of which have experienced widespread use). In order to solve the governing PDE, (2.2), we must first discretize $\mathbf{X}$, which leads to a system of ODEs. We then advance the solution to the system of ODEs in discrete time steps by employing a variable order solver based on the numerical differentiation formulas (NDFs) as implemented in Matlab's **ode15s**. In this study, we only consider uniform grids, so $\Delta x = \Delta x_i = x_{i+1} - x_{i,} \forall i$. To provide a sense for the subtle differences between the grids used with both approaches, as well as to provide a visual representation of the notation used throughout the rest of this study, we have included Figure 2.1. Note that $x_{mid(i)}$ is the midpoint between x_i and x_{i+1}.

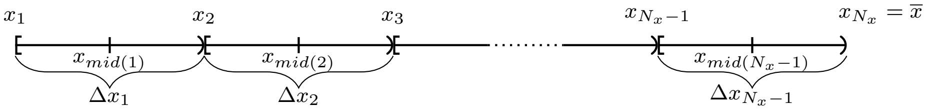

Figure 2.1: Discretization - Grid used for both FEM and FLFM where $\Delta x = \Delta x_i = x_{i+1} - x_i \forall i$. Only uniform grids are used in this study.

2.1.2 Finite Element Approach (FEM)

We now provide a brief overview of the important details of the FEM as discussed in Bortz et al. [20] and Ackleh and Fitzpatrick [2]. First we define our solution space as $H = L^1([\underline{x}, \overline{x}], \mathbb{R}_+)$, the space of integrable functions mapping a closed, bounded subset of positive reals into the positive reals where $\underline{x}$ and $\overline{x}$ are the respective minimum and maximum aggregate volumes. We use $N_x - 1$ elements in our numeric grid (see Figure 2.1), where each element boundary is denoted x_i for $i = 1, \ldots, N_x$ such that $x_1 = \underline{x}$ and $x_{N_x} = \overline{x}$. We then choose a set of hat basis functions for $i \in [1, N_x - 1]$

$$\beta_i^{N_x}(x) = \left\{ \begin{array}{ll} 1; & x_i^{N_x} \leq x < x_{i+1}^{N_x} \\ 0; & \text{otherwise} \end{array} \right\}$$

that form an orthogonal basis for our solution space

$$H^{N_x} = \left\{ h \in H : h = \sum_{i=1}^{N_x-1} \alpha_i \beta_i^{N_x}, \, \alpha_i \in \mathbb{R} \right\}.$$

The coefficients are $\alpha_j = \frac{1}{\Delta x} \int_{x_j}^{x_{j+1}} h(x)dx$, which allows us to define the projections $\pi^{N_x} : H \to H^{N_x}$ as

$$\pi^{N_x} h = \sum_{j=1}^{N_x-1} \alpha_j \beta_j^{N_x}$$

providing an orthogonal projection of H onto H^{N_x}. We can now approximate (2.2) with a set of $N_x - 1$ ODEs

$$\begin{aligned} f_t^{N_x} &= \pi^{N_x} \left(A(f^{N_x}) \right), \\ f^{N_x}(0, x) &= \pi^{N_x} \left(f(0, x) \right). \end{aligned} \tag{2.5}$$

The discretization described in (2.5) is a discontinuous Galerkin (DG) approximation using a zeroth order polynomial basis, and from Section 4 of [2], $f^{N_x} \to f$ uniformly in norm. As reported in [2], the FEM converges at first order on $L^\infty[\mathbf{X}]$. However, recent work by Yang and Shu in [91] on the supercovergence of DG methods and results from our numerical experiments support second order convergence in $L^1[\boldsymbol{X}]$. Future efforts will include an analytical investigation of the following conjecture.

Conjecture 1. *The approximate solution,* $f^{N_x}(t_k, x)$*, converges to the analytical solution with order 2 in* $L^1[\boldsymbol{X}]$*.*

Using this result, we note that the convergence of the ith moment is second order (or faster) in Δx.

Remark 2.1.1. *The* i^{th} *moment* $M_i^{N_x}$ *of the approximate solution converges to the* i^{th} *moment* M_i *of the analytical solution with order 2 (or faster) in* $L^1[\mathbf{X}]$*.*

Proof. Recall that for fixed t_k, there is second order convergence in Δx of f^{N_x} to f.

$$\begin{aligned}
\lim_{N_x\to\infty} \left| M_i^{N_x}(f(t_k,\cdot);\mathbf{X}) - M_i(f(t_k,\cdot);\mathbf{X}) \right| &= \lim_{N_x\to\infty} \left| \int_{\mathbf{X}} x^i f^{N_x}(t_k,x)dx - \int_{\mathbf{X}} x^i f(t_k,x)dx \right| \\
&= \lim_{N_x\to\infty} \left| \int_{\mathbf{X}} x^i \left\{ f^{N_x}(t_k,x) - f(t_k,x) \right\} dx \right| \\
&\leq \lim_{N_x\to\infty} \int_{\mathbf{X}} x^i \left| f^{N_x}(t_k,x) - f(t_k,x) \right| dx \\
&\leq \int_{\mathbf{X}} x^i dx \lim_{N_x\to\infty} \left\| f^{N_x}(t_k,x) - f(t_k,x) \right\|_{L^1[x_j,x_{j+1}]}
\end{aligned}$$

□

Before giving a detailed description of each term in the discretized system, we must highlight a few considerations. For the FEM, we use $f_i^{N_x}$ for $i \in [1, N_x - 1]$ to represent the discretized size distribution of aggregates in the i^{th} element. In our discretization scheme, the i^{th} element spans $[x_i, x_{i+1})$ with $x_1 = \underline{x}$ (depicted in Figure 2.1). For simplification of the explanations below, we let $x_1 = 0$. In the validation section, however, we compare our solution with an analytical solution to (2.2), which has a singularity at zero. Therefore in practice, we set $x_1 > 0$ in some scenarios (see Appendix D for a detailed discussion of the challenges associated with the value at which we start our grid). We then take the approach that all aggregates in a given element, i, have the discrete volume infinitesimally close to x_{i+1} with discretized size distribution, $f_i^{N_x}$. Under that rationale, no two aggregates can combine to produce one of size x_2, so the rate of change of $f_1^{N_x}$ is strictly negative. Furthermore, we account for the interactions of all particles with volumes up to $\overline{x}$. As mentioned above, the implication of this choice is that when two particles with volumes x_i and x_j aggregate to form a particle with volume $x_i + x_j$ and $x_i + x_j > x_{N_x} = \overline{x}$, we lose mass from our system.

We can now describe our discretized system fully. At $t = 0$, we project our initial conditions such that,

$$\pi^{N_x}(f(0,\cdot)) = \sum_{j=1}^{N_x-1} \alpha_j \beta_j^{N_x}(\cdot) \tag{2.6}$$

and for $x \in [x_i, x_{i+1})$

$$\sum_{j=1}^{N_x-1} \alpha_j \beta_j^{N_x}(x) = \frac{1}{\Delta x}\int_{x_i}^{x_{i+1}} f(0,y)dy.$$

Then for each discrete time step, t_k, we create two discretized vectors with $N_x - 1$ elements. The first vector represents aggregation of particles out of each element, while the second represents aggregation of particles into each element. These two vectors take on a different form for each of the two aggregation kernels ($K(x,y) \equiv 1$ and $K(x,y) = xy$) used in our study, and we present both vectors below. For aggregates which coagulate with an aggregate of size x to aggregates greater than size x, i.e., **aggregation out**,

$$A_{out}(f) = -f(x)\int_0^{\infty} K(x,y)f(y)dy.$$

To discretize this integral at each t_k, we have to truncate it to some finite maximum, $\overline{x}$. For the general aggregation kernel, $K(x,y)$, and for a given element, i,

$$\begin{aligned}
\pi^{N_x}\left(A_{out}(f_i^{N_x})\right) &= -\alpha_i \int_{x_1}^{\overline{x}} K(x_{i+1},y)\alpha(y)dy & (2.7)\\
&= -\alpha_i \sum_{j=1}^{N_x-1}\left(\int_{x_j}^{x_{j+1}} K(x_{i+1},y)\alpha(y)dy\right). & (2.8)
\end{aligned}$$

Now note that $\alpha_j = \frac{1}{\Delta x}\int_{x_j}^{x_{j+1}} h(x)dx = \frac{1}{\Delta x}\int_{x_j}^{x_{j+1}} f_j^{N_x}dx = f_j^{N_x}$ for any t_k where $k > 0$, therefore α_j is simply the approximated, discrete size distribution, $f_j^{N_x}$, from the previous time step. Then after making the appropriate substitutions and integrating, for $K(x,y) \equiv 1$,

$$\begin{aligned}
\pi^{N_x}\left(A_{out}(f_i^{N_x})\right) &= -\alpha_i \sum_{j=1}^{x_{nx}}\left(\int_{x_j}^{x_{j+1}} 1 \cdot \alpha_j dy\right)\\
&= -\alpha_i \sum_{j=1}^{nx-1} \alpha_j \triangle x.
\end{aligned}$$

therefore

$$\pi^{N_x}\left(A_{out}(f_i^{N_x})\right) = -f_i^{N_x}\Delta x \sum_{j=1}^{N_x-1} f_j^{N_x}, \tag{2.9}$$

and for $K(x,y) = xy$,

$$\begin{aligned}\pi^{N_x}\left(A_{out}(f_i^{N_x})\right) &= -\alpha_i \sum_{j=1}^{x_{nx}} \left(\int_{x_j}^{x_{j+1}} x_{i+1} y \alpha_j dy \right) \\ &= \frac{-\alpha_i x_{i+1}}{2} \left[\sum_{j=1}^{nx-1} \left(x_{j+1}^2 - x_j^2\right) \alpha_j \right],\end{aligned}$$

therefore,

$$\pi^{N_x}\left(A_{out}(f_i^{N_x})\right) = \frac{-f_i^{N_x} x_{i+1}}{2} \left[\sum_{j=1}^{N_x-1} \left(x_{j+1}^2 - x_j^2\right) f_j^{N_x} \right]. \tag{2.10}$$

We enter (2.9) and (2.10) for our respective **aggregation out** vectors. Now we consider the aggregates which coagulate to form an aggregate of size x, i.e., **aggregation in**. In the continuous case,

$$A_{in}(f) = \frac{1}{2} \int_0^x K(y, x-y) f(t,y) f(t,x-y) dy.$$

Discretizing this integral for the general aggregation kernel, $K(x,y)$, and for a given element, $i > 1$,

$$\begin{aligned}\pi^{N_x}\left(A_{in}(f_i^{N_x})\right) &= \frac{1}{2} \int_{x_1}^{x_i} K(y, x_i - y) \alpha(y) \alpha(x_i - y) dy &(2.11)\\ &= \frac{1}{2} \sum_{j=1}^{i-1} \int_{x_j}^{x_{j+1}} K(y, x_i - y) \alpha_j \alpha(x_i - y) dy &(2.12)\end{aligned}$$

Again note that $\alpha_j = \frac{1}{\Delta x} \int_{x_j}^{x_{j+1}} h(x) dx = \frac{1}{\Delta x} \int_{x_j}^{x_{j+1}} f_j^{N_x} dx = f_j^{N_x}$ for any t_k where $k > 0$, therefore α_j is simply the approximated, discrete size distribution, $f_j^{N_x}$, from the previous time step. Then after making the appropriate substitutions and integrating for $K(x,y) \equiv 1$,

$$\pi^{N_x}\left(A_{in}(f_i^{N_x})\right) = \frac{1}{2} \Delta x \sum_{j=1}^{i-1} 1 \cdot \alpha_j \alpha_{i-j},$$

therefore

$$\pi^{N_x}\left(A_{in}(f_i^{N_x})\right) = \frac{1}{2} \Delta x \sum_{j=1}^{i-1} f_j^{N_x} f_{i-j}^{N_x}, \tag{2.13}$$

and for $K(x,y) = xy$,

$$\begin{aligned}\pi^{N_x}\left(A_{in}(f_i^{N_x})\right) &= \frac{1}{2} \sum_{j=1}^{i-1} \left(\int_{x_j}^{x_{j+1}} y \cdot (x_i - y) \alpha_j \alpha_{i-j} dy \right) \\ &= \frac{1}{2} \sum_{j=1}^{i-1} \left[x_i \frac{x_{j+1}^2 - x_j^2}{2} - \frac{x_{j+1}^3 - x_j^3}{3} \right] \alpha_j \alpha_{i-j},\end{aligned}$$

therefore

$$\pi^{N_x}\left(A_{in}(f_i^{N_x})\right) = \frac{1}{2} \sum_{j=1}^{i-1} \left[x_i \frac{x_{j+1}^2 - x_j^2}{2} - \frac{x_{j+1}^3 - x_j^3}{3} \right] f_j^{N_x} f_{i-j}^{N_x}. \tag{2.14}$$

We enter (2.13) and (2.14) for our respective **aggregation in** vectors.

For the vectors above, we offer the following derivation. In our discretization scheme, the first bin starts at $x_1 = \underline{x}$ and ends infinitely close to x_2. We then take the approach that all aggregates in that bin have the discrete value infinitesimally close to x_2 with density $f_1^{N_x}$. Under that rationale, no two aggregates can produce one of size x_2, so we can only reduce the density of the first bin, hence $f_1^{N_x}$ is strictly negative. Furthermore, aggregates in the first bin, considered to have volume x_2, can coagulate with any other sized aggregate up to x_{N_x}, so we account for each of those interactions. To illustrate, we describe the interaction of aggregates in the first bin with aggregates in the second bin as $-\alpha_1 \int_{x_2}^{x_3} K(x_2, y)\alpha(y)dy$, which creates an aggregate infinitesimally smaller than x_4 and decreases the density of aggregates of the first bin, $f_1^{N_x}$. Note that at each time step, the densities of each bin are a real number, hence α_j is simply the approximated density, $f_j^{N_x}$, at the previous time step. Finally, in our summation of the interactions between aggregates that increase the density of a certain bin, we multiply by 1/2 to account for double counting. For instance, consider the density of the third bin. The terms that increase that density are represented by the sum,

$$\frac{1}{2}\sum_{j=1}^{2}\int_{x_j}^{x_{j+1}} K(y, x_3 - y)\alpha_j \alpha(x_3 - y)dy = \frac{1}{2}\sum_{j=1}^{2}\left[x_3\frac{x_{j+1}^2 - x_j^2}{2} - \frac{x_{j+1}^3 - x_j^3}{3}\right] f_j^{N_x} f_{3-j}^{N_x}.$$

2.1.3 Filbet and Laurençot Flux Method (FLFM)

Our second approach for numerically solving the Smoluchowski coagulation equation is a scheme developed by Filbet and Laurençot in [43]. They base their scheme on a finite volume method and calculate a mass flux quantity, which we denote, $J[f](t, x)$. Here, $J[f](t, x)$ represents a mass flux from aggregates with volumes at most x to aggregates with volumes greater than x. Then similar to Filbet and Laurençot, we reformulate [43, 65] the Smoluchowski coagulation equation (2.2)

$$x\partial_t f = -\partial_x J[f],\ (t, x) \in \mathbb{R}_+^2 \tag{2.15}$$

where

$$J[f](t, x) = \int_0^x \int_{x-u}^{\infty} uK(u, v)f(t, u)f(t, v)dvdu,\ x \in \mathbb{R}_+;\ t \in \mathbb{R}_+. \tag{2.16}$$

We can recover the conventional formulation of the Smoluchowski coagulation equation, (2.2), by substituting (2.16) into (2.15) and applying Leibniz's rule. Once again, for numerical purposes, we must truncate the volume variable, x, to a finite value, $\overline{x}$. Filbet and Laurençot [43] describe a number of choices (conservative and nonconservative) for truncating the inner integral in (2.16). We follow their recommendation by using the nonconservative formulation

$$J[f](t,x) = \int_0^x \int_{x-u}^{\overline{x}} uK(u,v)f(t,u)f(t,v)dvdu,\ x \in (0,\overline{x});\ t \in \mathbb{R}_+ \tag{2.17}$$

because it generates accurate approximations when solutions include gelation [6, 26, 43]. As mentioned in [43], we can rewrite (2.15) in terms of a volume distribution, which we denote $g(t,x) = xf(t,x)$. Then (2.15) and (2.16) become

$$\partial_t g = -\partial_x J[g],\ (t,x) \in \mathbb{R}_+^2 \tag{2.18}$$

and

$$J[g](t,x) = \int_0^x \int_{x-u}^{\overline{x}} \frac{K(u,v)}{v} g(t,u)g(t,v)dvdu,\ x \in (0,\overline{x});\ t \in \mathbb{R}_+. \tag{2.19}$$

This formulation is especially useful in application when the data has the form of a volume distribution, and we discuss the advantages of this formulation in more detail in Section 2.3.2.

Numerically solving the formulation in (2.15) differs fundamentally from numerically solving the formulation for which we used finite elements. With FEM, we track the changes in size distribution for given elements. With the formulation in (2.15), we track the discretized volume distribution, which we denote, $g_i^{N_x}(t_k)$, representing the approximated mean value of $g(t_k,x)$ in the element, $[x_i, x_{i+1})$ at discrete time steps, t_k. This formulation also includes the discretized mass flux, which we denote, $J_i^{N_x}(t_k)$, across element boundaries (recall Figure 2.1 with boundaries, x_i) at discrete time steps. To understand how we determine the flux, $J_i^{N_x}(t_k)$, at each element boundary, x_i, for any time step, consider the following. First, $J_1^{N_x}(t_k) = 0\,\forall k$, and for all other element boundaries, flux across a given boundary, x_r, requires $x_{mid(i)} + \tilde{x} \geq x_r$. We now fix x_r and $x_{mid(i)} < x_r$ to determine the discretized volumes, $x_{mid(j)}$, that are equal to or larger than $\tilde{x}$. For each j such that this is true, the aggregation of $x_{mid(i)} + x_{mid(j)}$ adds to flux across x_r. Therefore the discretized flux contributed to $J_r^{N_x}(t_k)$ by $x_{mid(i)}$ and a given $x_{mid(j)}$ is

$$\Delta x g_i^{N_x}(t_k) \int_{x_j}^{x_{j+1}} \frac{K(x_{mid(i)}, y)}{y} g_j^{N_x}(t_k)dy,$$

and we can simply sum across all j for which $x_{mid(j)} \geq \tilde{x}$. The small exception to this rule occurs for the lowest j. In that case, the lower limit of integration is $x_{mid(j)}$ instead of x_j.

Now we can use the FLFM to solve the Smoluchowski equation. For consistency, N_x represents the number of element boundaries, where each element boundary is denoted x_i for $i = 1, \ldots, N_x$ such that

$x_1 = \underline{x}$ and $x_{N_x} = \overline{x}$. Again we only consider uniform grids, so $\Delta x = \Delta x_i = x_{i+1} - x_i \, \forall i$. Then at each time step and at each element midpoint, we approximate (2.18) with

$$\frac{g_i^{N_x}(t_{k+1}) - g_i^{N_x}(t_k)}{\Delta t} = \frac{J_{i+1}^{N_x}(t_k) - J_i^{N_x}(t_k)}{\Delta x},\ i \in [1, N_x - 1] \tag{2.20}$$

and we approximate our initial conditions with

$$g_i^{N_x}(0) = \frac{1}{\Delta x}\int_{x_i}^{x_{i+1}} x f(0,x)dx. \tag{2.21}$$

Now recall that $J[g]$ is defined as $\int_0^x \int_{x-u}^{\overline{x}} \frac{K(u,v)}{v} g(t,u)g(t,v)dvdu$ with $x \in (0, \overline{x})$ and $t \in \mathbb{R}_+$, so evaluation of the right hand side of (2.20) is less obvious. To illustrate how we calculate the right hand side of our second order approximation in (2.20), we present it in Appendix A. In [43], Filbet and Laurençot demonstrate second order convergence in Δx of the FLFM in the L^1 norm. Using similar arguments as those made in Section 2.1.2, we note the convergence of the i^{th} moments is second order (or faster) in Δx.

Remark 2.1.2. *The i^{th} moment $M_i^{N_x}$ of the approximate solution converges to the i^{th} moment M_i of the analytical solution with order 2 (or faster) in $L^1[\mathbf{X}]$.*

Proof. Recall that for fixed t_k, there is second order convergence in Δx of g^{N_x} to g.

$$\begin{aligned}
\lim_{N_x\to\infty} \left| M_i^{N_x}(f(t_k,\cdot);\mathbf{X}) - M_i(f(t_k,\cdot);\mathbf{X}) \right| &= \lim_{N_x\to\infty} \left| \int_{\mathbf{X}} x^i f^{N_x}(t_k,x)dx - \int_{\mathbf{X}} x^i f(t_k,x)dx \right| \\
&= \lim_{N_x\to\infty} \left| \int_{\mathbf{X}} x^{i-1} g^{N_x}(t_k,x)dx - \int_{\mathbf{X}} x^{i-1} g(t_k,x)dx \right| \\
&= \lim_{N_x\to\infty} \left| \int_{\mathbf{X}} x^{i-1} \left\{ g^{N_x}(t_k,x) - g(t_k,x) \right\} dx \right| \\
&\le \lim_{N_x\to\infty} \int_{\mathbf{X}} x^{i-1} \left| g^{N_x}(t_k,x) - g(t_k,x) \right| dx \\
&\le \int_{\mathbf{X}} x^{i-1} \lim_{N_x\to\infty} \left\| g^{N_x}(t_k,x) - g(t_k,x) \right\|_{L^1[x_j,x_{j+1}]}
\end{aligned}$$

$\square$

2.2 Analytical Solutions

In Figure 2 of [89], Wattis provides a diagram partitioning regions of different generic behavior for varying aggregation kernels with general form $K(x,y) = x^\mu y^\nu + x^\nu y^\mu$ where $\mu, \nu \in \mathbb{R}_+$, including the exactly solvable cases. Lee generates similar conclusions with respect to the generic behavior for varying aggregation kernels in [57]. In order to make fair comparisons between the FEM and the FLFM, we use known solutions to (2.2) for the two aggregation kernels, $K(x,y) \equiv 1$ and $K(x,y) = xy$. The aggregation kernel, $K(x,y) \equiv 1$, represents a system with slower aggregation and no gelation, while $K(x,y) = xy$ represents a system with rapid aggregation where gelation does occur. By including both kernels, not only can we compare the FEM and FLFM to known solutions, but we cover a breadth of possible systems. We also recognize that the information lost in the interval $[0, x_1)$ degrades the overall accuracy of the respective methods, and we address this in more detail in Section 2.3.1.

A known analytical solution for $K(x,y) \equiv 1$ is [43]

$$f(t,x) = \left(\frac{2}{2+t}\right)^2 e^{-\frac{2}{2+t}x}. \tag{2.22}$$

We depict the solution (2.22) in Figure 2.2a for several different snapshots in time. Similarly, a known analytical solution for $K(x,y) = xy$ is [39,43]

$$f(t,x) = e^{(-T(t)x)} \frac{I_1(2x\sqrt{t})}{x^2\sqrt{t}}. \tag{2.23}$$

Here

$$T(t) = \begin{cases} 1+t & \text{if } t \leq 1 \\ 2\sqrt{t} & \text{otherwise} \end{cases},$$

and

$$I_1(x) = \frac{1}{\pi}\int_0^{\pi} e^{x\cos\theta}\cos\theta d\theta$$

is a modified Bessel function of the first kind. We depict in Figure 2.2b the solution (2.23) for several different snapshots in time. For this solution, note that $f(0,x) = \frac{e^{-x}}{x}$, which is not necessarily obvious (see Appendix B for the derivation).

(a) $K(x,y) \equiv 1$

(b) $K(x,y) = xy$

Figure 2.2: Analytic solutions - size distribution, $f(t,x)$, vs volume, x, for several snapshots in time: $t = 0$, $t = 0.5$, $t = 1$, and $t = 3$ in semilog scale. We use $K(x,y) \equiv 1$ and $K(x,y) = xy$ as the two aggregation kernels representing a breadth of modeled systems from which we can base comparisons of the two methods studied, the FEM and the FLFM.

2.3 Computational Results

Using the analytical solutions described in the previous section, we can test both numeric schemes, the FEM and the FLFM, to compare their results. In Section 2.3.1, we define our measure of error and compare the resulting convergence rates achieved by both methods. In Section 2.3.2, we compare the FEM's and the FLFM's accuracy in approximating the zeroth and first moments. In Section 2.3.3, we discuss the computation cost required for each of our simulations. Finally, in Section 2.3.4, we examine the effects of grid spacing and our truncation parameter, $\overline{x}$.

2.3.1 Validation

We cannot overstate the importance of computing the correct norm when determining the error in a particular numerical scheme. In particular, when using the FEM, we approximate f, but using the FLFM, we approximate g. We then denote the mean analytical solution across the i^{th} element at t_k as $f_i(t_k)$ and $g_i(t_k)$ respectively. To compute the error for both methods, we use the grid function norm[2] . For the FEM, we denote the error

$$e_i(t_k) = \left| f_i^{N_x}(t_k) - \frac{M_0(f(t_k,\cdot);x_i,x_{i+1})}{\Delta x} \right| = \left| f_i^{N_x}(t_k) - \pi^{N_x}(f(t_k)) \right|$$

---

[2] See Appendix A.5 of LeVeque [59] for further details.

and for the FLFM, we denote the error

$$e_i(t_k) = \left| g_i^{N_x}(t_k) - \frac{M_1(\frac{g(t_k,\cdot)}{\cdot}; x_i, x_{i+1})}{\Delta x} \right| = \left| g_i^{N_x}(t_k) - g_i(t_k) \right|.$$

In both cases, we generate vectors discretizing an error function, $e(t_k, x)$, so we calculate the grid function norm as

$$\|e(t_k)\|_1 = \Delta x \sum_{i=1}^{N_x - 1} e_i(t_k).$$

With our error defined, we aim to reduce the impact of information lost from excluding the interval $[0, x_1)$ by using the domain $t = [1, 3]$. We now compare the accuracy of the two methods for each aggregation kernel, and we plot the results in Figures 2.3 and 2.4.

When $K(x, y) \equiv 1$, the average analytical solution across the i^{th} element is

$$\begin{aligned} f_i(t_k) &= \frac{1}{\Delta x} \int_{x_i}^{x_{i+1}} \left(\frac{2}{2+t} \right)^2 e^{-(\frac{2}{2+t})y} dy \\ &= \frac{1}{\Delta x} \left(-\frac{2}{2+t} \right) \left[e^{-\frac{2x_{i+1}}{2+t}} - e^{-\frac{2x_i}{2+t}} \right], \end{aligned}$$

from which we calculate the error in the FEM. Conversely, when we calculate the error in the FLFM, the analytical solution across the i^{th} element is

$$\begin{aligned} g_i(t_k) &= \frac{1}{\Delta x} \int_{x_i}^{x_{i+1}} \left(\frac{2}{2+t} \right)^2 y e^{-(\frac{2}{2+t})y} dy \\ &= \frac{1}{\Delta x} \int_{x_i}^{x_{i+1}} \left(\frac{2}{2+t} \right) \left(\frac{2y}{2+t} \right) e^{-(\frac{2y}{2+t})} dy \\ &= \frac{1}{\Delta x} \int_{x_i}^{x_{i+1}} u e^{-u} du \\ &= \frac{1}{\Delta x} (u+1) \left(-e^{-u} \right) \Big|_{x_i}^{x_{i+1}} \\ &= \frac{1}{\Delta x} \left[\left(\frac{2x_i}{2+t} + 1 \right) \left(e^{-\frac{2x_i}{2+t}} \right) - \left(\frac{2x_{i+1}}{2+t} + 1 \right) \left(e^{-\frac{2x_{i+1}}{2+t}} \right) \right]. \end{aligned}$$

With $K(x, y) \equiv 1$, x_1 can be as small as we wish, but physically, $x_1 > 0$, so we choose $x_1 = 10^{-3}$. We should also note that for any choice of $x_1 > 0$, we introduce error by disregarding information generated in the true solution by volumes in the range $[0, x_1)$. Under these conditions, we achieve approximately first order accuracy using the finite element approach as depicted in Figure 2.5. We achieve approximately 1.5 order accuracy using the flux approach, also depicted in Figure 2.5, and the overall error is much smaller.

When $K(x, y) = xy$, to calculate error in the FEM approach, we use the average analytical solution across the i^{th} element

$$f_i(t_k) = \frac{1}{\Delta x}\int_{x_i}^{x_{i+1}} e^{(-Ty)}\frac{I_1(2y\sqrt{t})}{y^2\sqrt{t}}dy. \tag{2.24}$$

To calculate the error in the FLFM approach, we use the average analytical solution across the i^{th} element

$$g_i(t_k) = \frac{1}{\Delta x}\int_{x_i}^{x_{i+1}} e^{(-Ty)}\frac{I_1(2y\sqrt{t})}{y\sqrt{t}}dy. \tag{2.25}$$

Neither (2.24) or (2.25) have analytic integrals, so we apply global adaptive quadrature, as implemented in Matlab's **integral2**, with the default relative tolerance of 10^{-6} and absolute tolerance of 10^{-10}, to approximate f_i and g_i respectively at each time step. Additionally, extremely small volume sizes create large numerical inaccuracies in these integrals, so to achieve the best results, we choose $x_1 = 0.75$. Under these assumptions, we achieve approximately 0.3 order accuracy using the FEM approach, whereas we achieve approximately first order accuracy using FLFM as depicted in Figure 2.5. For both methods, and with both aggregation kernels, we achieve less accuracy than the maximum achievable by the respective methods, which we address below.

(a) FEM

(b) FLFM

Figure 2.3: Error vs. Time - L^1 grid error norm vs. time when $K(x, y) \equiv 1$ for increasing grid densities: $N_x = 100$, $N_x = 200$, and $N_x = 400$ in linear scale. We define the error for the FEM based on the difference between analytic and numeric size distribution, f, but we base the error for the FLFM on the difference between analytic and numeric volume distribution, xf. The FLFM provides a higher order of accuracy with this aggregation kernel, which represents a system that aggregates slowly and does not experience gelation.

(a) FEM

(b) FLFM

Figure 2.4: Error vs. Time - L^1 grid error norm vs. time when $K(x, y) = xy$ for increasing grid densities: $N_x = 100$, $N_x = 200$, and $N_x = 400$ in linear scale. We define the error for the FEM based on the difference between analytic and numeric size distribution, f, but we base the error for the FLFM on the difference between analytic and numeric volume distribution, xf. The FLFM provides a higher order of accuracy than FEM as well for this aggregation kernel, which represents a rapidly aggregating system where gelation occurs.

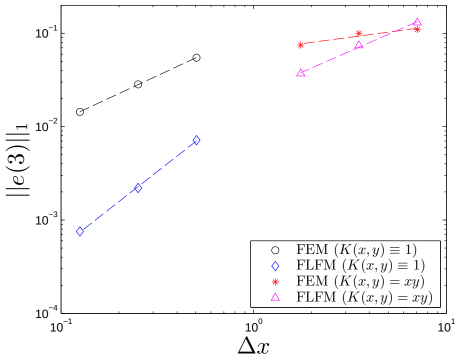

Figure 2.5: Error vs. Δx - L^1 grid error norm at $t = 3$ vs. Δx in log scale for both the FEM and the FLFM using both aggregation kernels, $K(x, y) \equiv 1$ and $K(x, y) = xy$. The slope of the dashed lines represent the approximate order of accuracy of each method using each respective aggregation kernel. The FEM achieves approximately first and 0.3 order accuracy for the kernels $K(x, y) \equiv 1$ and $K(x, y) = xy$ respectively. The FLFM achieves approximately 1.5 and first order for the kernels $K(x, y) \equiv 1$ and $K(x, y) = xy$ respectively.

Undoubtedly, the information lost in the interval $[0, x_1)$ degrades the overall accuracy of the respective methods. In light of these inaccuracies, we offer another test of the methods' convergence rates for both aggregation kernels. In this second test, we compare solutions for both kernels using 100, 200, 400, 800, and 1600 points to a fine grid solution of 3200 points.[3] The error here is analogous to the error measured

---

[3] Due to the large computation time required by the FLFM when $K(x, y) = xy$, we currently present that case's results for 100, 200, 400, and 800 grid points compared to a fine grid solution of 1600 points in Figure 2.6.

when we compare our approximated solutions for varying N_x to the analytic solution. In the interest of clarity, we use a superscript, *, to denote the error measured when we compare our approximated solutions for varying N_x to the fine grid solution where $N_x = 3200$. For the FEM, we then denote the error

$$e_i^*(t_k) = \left| f_i^{N_x}(t_k) - f_i^{3200}(t_k) \right|,$$

and for the FLFM, we denote the error

$$e_i^*(t_k) = \left| g_i^{N_x}(t_k) - g_i^{3200}(t_k) \right|.$$

In both cases, we generate vectors discretizing an error function, $e^*(t_k, x)$, so we calculate the grid function norm as

$$\|e^*(t_k)\|_1 = \Delta x \sum_{i=1}^{N_x - 1} e_i^*(t_k).$$

With this test, we achieve an order of accuracy that trends towards second order with each doubling of the number of grid points. These results support our conjecture of second order accuracy for the FEM and support the work in [43] that demonstrates second order accuracy for the FLFM. We depict these results in Figure 2.6.

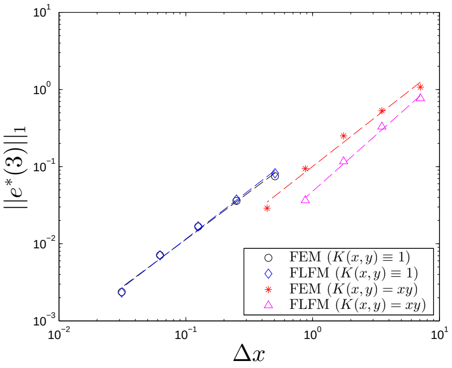

Figure 2.6: Error vs. Δx - L^1 grid error norm at $t = 3$ vs. Δx in log scale for both the FEM and the FLFM using the aggregation kernel, $K(x, y) = xy$. The slope of the dashed lines represents the approximate order of accuracy of each method. Both methods trend towards approximately second order accuracy.

2.3.2 Moment calculations

In this section, we investigate both methods' accuracy in approximating the moments. Our study reveals that an inherent advantage of the FEM in its use of a size distribution results in a much more accurate approximation of the zeroth moment when $K(x,y) \equiv 1$. Conversely, the FLFM's use of a volume distribution results in a more accurate approximation of the first moment for both aggregation kernels.

Mathematically, we represent total aggregates as the zeroth moment, M_0, and total volume as the first moment, M_1, as defined in (1.1). Different formulations of the governing Smoluchowski equation induce different approaches to calculating the moments numerically. For example, Guy, Fogelson, and Keener [47] extend the generating function approach described in [93] to study blood clots. In the FEM approach, we approximate the size distribution across the i^{th} element as $f_i^{N_x}(t_k)$, whereas with the FLFM, we approximate the volume distribution across the i^{th} element as $g_i^{N_x}(t_k)$. Using (1.1) with our known analytical solutions for $f(t,x)$, the analytical total number of particles in our truncated system is

$$M_0(t_k) = \int_{x_1}^{x_{N_x}} f(t_k,y)dy = \int_{x_1}^{x_{N_x}} \frac{g(t_k,y)}{y}dy, \tag{2.26}$$

and the analytical total volume in our truncated system is

$$M_1(t_k) = \int_{x_1}^{x_{N_x}} yf(t_k,y)dy = \int_{x_1}^{x_{N_x}} g(t_k,y)dy. \tag{2.27}$$

We acknowledge the mild abuse of the notation in redefining M_i in (2.26) and (2.27) in the name of focusing attention on how the moment changes as a function of time. In what follows we will clearly note when referring to moments of the FEM or the FLFM solutions. We demonstrate below that the FEM more accurately approximates the zeroth moment when $K(x,y) \equiv 1$.

Through contrasting our approximations of the zeroth moment by the two methods studied in this paper, we derive an important advantage that the FEM possesses at $t = 0$ for a slowly aggregating system (e.g., $K(x,y) \equiv 1$). In this case, for the FEM,

$$M_0^{N_x}(t_k) = \sum_{i=1}^{N_x-1} \int_{x_i}^{x_{i+1}} e^{-y}dy = M_0(0),$$

but for the FLFM

$$M_0^{N_x}(0) = \sum_{i=1}^{N_x-1} \left[\left(\frac{1}{\Delta x} \left\{ (x_i+1)\, e^{-x_i} - (x_{i+1}+1)\, e^{-x_{i+1}} \right\} \right) \ln\left(\frac{x_{i+1}}{x_i} \right) \right] \approx M_0(0).$$

To derive this result, we start with the general formulation of the zeroth moment at t_k. For the FEM,

$$M_0^{N_x}(t_k) = \int_{x_1}^{x_{N_x}} f_i^{N_x}(t_k)dy = \Delta x \sum_{i=1}^{N_x-1} f_i^{N_x}(t_k),$$

whereas with the FLFM

$$M_0^{N_x}(t_k) = \int_{x_1}^{x_{N_x}} \frac{g_i^{N_x}(t_k)}{y} dy = \sum_{i=1}^{N_x-1} \left[g_i^{N_x}(t_k) \ln\left(\frac{x_{i+1}}{x_i}\right) \right].$$

Then at $t = 0$ and with $K(x,y) \equiv 1$, we have $f(0,x) = e^{-x}$ and $g(0,x) = xe^{-x}$, which we initialize numerically via (2.6) and (2.21) respectively. The analytical zeroth moment,

$$M_0(0) = \int_{x_1}^{x_{N_x}} f(0,y) dy = \sum_{i=1}^{N_x-1} \int_{x_i}^{x_{i+1}} e^{-y} dy,$$

matches the approximation by the FEM,

$$M_0^{N_x}(0) = \int_{x_1}^{x_{N_x}} f_i^{N_x}(0) dy = \Delta x \sum_{i=1}^{N_x-1} f_i^{N_x}(0) = \sum_{i=1}^{N_x-1} \int_{x_i}^{x_{i+1}} e^{-y} dy.$$

Conversely, the approximation by the FLFM,

$$\begin{aligned} M_0^{N_x}(0) &= \int_{x_1}^{x_{N_x}} \frac{g_i^{N_x}(0)}{y} dy = \sum_{i=1}^{N_x-1} \left[g_i^{N_x}(0) \ln\left(\frac{x_{i+1}}{x_i}\right) \right] \\ &= \sum_{i=1}^{N_x-1} \left[\left(\frac{1}{\Delta x} \left\{ (x_i+1) e^{-x_i} - (x_{i+1}+1) e^{-x_{i+1}} \right\} \right) \ln\left(\frac{x_{i+1}}{x_i}\right) \right], \end{aligned}$$

is clearly not the same as $M_0(0)$. Not surprisingly, our outputs for $M_0^{N_x}(0)$ vary slightly in Figure 2.7a such that $M_0^{N_x}(0) = M_0(0) \approx 0.999$ using the FEM, but $M_0^{N_x}(0) \approx 1.169$ using the FLFM. Along similar lines, when $K(x,y) = xy$, we have $M_0(0)$ matching the approximation by the FEM where $M_0^{N_x}(0) \approx 0.34$, but the FLFM produces $M_0^{N_x}(0) \approx 0.2916$ as depicted in Figure 2.7b. We summarize these results in Table 2.1. Clearly, with experimental data in the form of a size distribution, the FLFM starts at a disadvantage approximating the zeroth moment since its approximation at $t = 0$ contains error. Furthermore, the FEM maintains a better approximation of the zeroth moment as depicted in Figure 2.8a.

Now contrasting our approximations of the first moment, we demonstrate more accuracy by the FLFM than by the FEM. Using the FEM,

$$M_1^{N_x}(t_k) = \int_{x_1}^{x_{N_x}} y f(t_k,y) dy \approx \frac{1}{2} \sum_{i=1}^{N_x-1} f_i^{N_x}(t_k)(x_{i+1}^2 - x_i^2),$$

whereas using the FLFM,

$$M_1^{N_x}(t_k) \approx \int_{x_1}^{x_{N_x}} g_i^{N_x}(t_k) dy = \Delta x \sum_{i=1}^{N_x-1} g_i^{N_x}(t_k).$$

In this case, with $t = 0$ and $K(x, y) \equiv 1$, $M_1^{N_x}(0) = M_1(0) \approx 1.0000$ using the FLFM, but $M_1^{N_x}(0) \approx 1.0013$ using the FEM. Similarly, when $t = 0$ and $K(x, y) = xy$, $M_1(0)$ matches the approximation using the FLFM where $M_1^{N_x}(0) \approx 0.472$, but the FEM produces $M_1^{N_x}(0) \approx 0.602$. We summarize these results in Table 2.1.

(a) $K(x, y) \equiv 1$

(b) $K(x, y) = xy$

Figure 2.7: $M_0^{400}(t)$ vs. Time - Numerical approximation of the zeroth moment for a truncated volume domain, x_1 to x_{400}, for both aggregation kernels. Note, with the FEM, $M_0^{400}(0) = M_0(0)$, but with the FLFM, $M_0^{400}(0) \approx M_0(0)$. When given data in the form of a size distribution, the FEM's approximation of the total particles in a system starts with an advantage over the FLFM's approximation, which has error at $t = 0$. We use a linear scale for both plots.

	Analytical	FEM	FLFM
$M_0(0)$	0.999	0.999	1.169
$M_1(0)$	1.0000	1.0013	1.0000

(a) $K(x, y) \equiv 1$

	Analytical	FEM	FLFM
$M_0(0)$	0.34	0.34	0.2916
$M_1(0)$	0.472	0.602	0.472

(b) $K(x, y) = xy$

Table 2.1: Comparison of analytical partial i^{th} moments ($i = 0, 1$) at $t = 0$ with the approximations by both the FEM and the FLFM. The analytical $M_0(0)$ exactly matches that of the FEM, but the FLFM's approximation of $M_0(0)$ contains error. Conversely, the analytical $M_1(0)$ exactly matches that of the FLFM, but the FEM's approximation of $M_1(0)$ contains error.

Having illuminated the respective advantages the FEM has approximating the zeroth moment, and the FLFM has approximating the first moment, we now examine the convergence rates of the two methods to a fine grid ($N_x = 3200$) approximation of the moments. In this case, we compute the difference between the lower resolution grid ($N_x = 100, 200, 400, 800, 1600$) approximations of the moments at $t = 3$, and the fine grid ($N_x = 3200$) approximation.[4] We denote the difference in the approximations of the zeroth moment, M_0^{diff}, and the difference in the approximations of the first moment, M_1^{diff} where

$$\begin{aligned} M_0^{diff} &= \left| M_0^{N_x}(3) - M_0^{3200}(3) \right| \\ M_1^{diff} &= \left| M_1^{N_x}(3) - M_1^{3200}(3) \right|. \end{aligned}$$

Our simulations include both aggregation kernels, and we depict the convergence rates in Figures 2.8a and 2.8b. As expected, for both methods, we observe a trend towards second order accuracy (more evidence supporting our claim of second order convergence for the FEM). Intriguingly, when $K(x, y) \equiv 1$, the FEM more accurately predicts the zeroth moment. In this case, given experimental data in the form of a size distribution and a system experiencing slow aggregation, the FEM is a better choice of methods. We summarize convergence rates of these simulations in Table 2.2, and note that as the number of grid points double the convergence rates tend toward the expected convergence rates described in Sections 2.1.2 and 2.1.3.

	Method	Moment	100→200	200→400	400→800	800→1600
$K \equiv 1$	FEM	Zeroth	0.2	1.1	1.2	1.4
		First	1.1	1.1	1.2	1.6
	FLFM	Zeroth	1.2	1.3	1.5	1.8
		First	0.6	1.4	1.7	2
$K = xy$	FEM	Zeroth	0.2	0.5	1.3	1.6
		First	0.5	1.0	1.0	1.5
	FLFM	Zeroth	0.7	1.5	1.4	*[5]
		First	1.4	6.6	*[5]	*[5]

Table 2.2: Convergence rates of coarse grid (N_x = 100, 200, 400, 800, 1600) approximations of the zeroth and first moments to a fine grid ($N_x = 3200$) approximation of the moments. In all cases, we observe a trend towards second order convergence.

---

[4] Due to the large computation time required by the FLFM when $K(x, y) = xy$, we currently present that case's results for 100, 200, 400, and 800 grid points compared to a fine grid solution of 1600 points in Table 2.2 and Figure 2.8.

[5] Results not reported due to limitations of machine precision and available computational resources

(a) Zeroth Moment

(b) First Moment

Figure 2.8: Moment differences at $t = 3$ vs. Δx - Difference between approximations of the zeroth and first moments by coarse grid ($N_x = 100$, 200, 400, 800, 1600) simulations and the approximation by the fine grid ($N_x = 3200$) simulation. In all cases, we observe a trend towards second order convergence, with one case (slow aggregation, e.g., $K(x, y) \equiv 1$ and zeroth moment approximation) where the FEM is more accurate.

2.3.3 Computation cost

Clearly, order of accuracy is important, but we also want to know which method requires more computation in terms of floating point operations. To make the comparisons, we compute the floating point operations for the simulations discussed in Section 2.3.1 for both the FEM and the FLFM. The number of operations counted includes only the computations required for each algorithm to solve the system of ODEs at a given point in time, t_k. We implement the simulations using Matlab version 2013a on an Intel(R) Core(TM) i-5 2410M CPU @ 2.3 GHz. For each simulation, the FEM requires significantly less floating point operations than the FLFM. The results are summarized in Table 2.3 and give us important insights. When $K(x, y) \equiv 1$, the required number of floating point operations and an extrapolation of the error data in Figure 2.5 imply that the FEM with 800 grid points can achieve nearly equal accuracy as the FLFM with 100 grid points. The FEM achieves this accuracy with only 38% of the floating point operations that it takes the FLFM, so when computation cost is more valuable to the user, the FEM provides a better choice.

		$N_x = 100$	$N_x = 200$	$N_x = 400$	$N_x = 800$
$K(x, y) \equiv 1$	FEM	1.46×10^4	5.93×10^4	2.39×10^5	9.57×10^5
	FLFM	2.49×10^6	1.99×10^7	1.60×10^8	1.28×10^9
$K(x, y) = xy$	FEM	6.71×10^4	2.74×10^5	1.11×10^6	4.46×10^6
	FLFM	2.48×10^6	1.99×10^7	1.60×10^8	1.28×10^9

Table 2.3: Comparison of floating point operations required to solve the right hand side system of ODEs for any t_k for both the FEM and the FLFM. We perform the simulations on a 2.3 GHz processor. When $K(x, y) \equiv 1$, the number of floating point operations performed for the FEM simulation with 800 grid points requires only 38% of the number of floating point operations that the FLFM simulation with 100 grid points requires. The error is nearly the same for both simulations implying that if computation cost is more valuable to the user, the FEM should be the choice of methods.

2.3.4 Relationship between $\overline{x}$ and Δx

In [43], Filbet and Laurençot report sensitivity of the FLFM to the truncation parameter, $\overline{x}$. We study the error as a function of both $\overline{x}$ and Δx, and in particular, we would like determine to what extent the truncation parameter, $\overline{x}$, impacts the overall accuracy of the two schemes. We do not find the following results conclusive, but they do reveal intriguing patterns that we plan to study more extensively in future work.

Note that for each run and a given value of $\overline{x}$, we initialize our grid with $x_1 = 0.001$ when $K(x, y) \equiv 1$ and with $x_1 = 0.75$ when $K(x, y) = xy$. Notice in Figures 2.9 and 2.10, for a given Δx, using both the FEM and the FLFM, the error is the same regardless of the value of $\overline{x}$ for both kernels, and we achieve the expected behavior of decreasing error with refinement of the grid. We suggest that when $K(x, y) \equiv 1$ with the initial conditions used in this study, the analytic solutions decay so quickly that the numeric approximations do not suffer greatly from the truncation parameter, $\overline{x}$, for either method as evidenced in Figure 2.9. However, when $K(x, y) = xy$, we cannot make the same general statement. Using the FLFM with $\overline{x} = 80$, $\overline{x} = 160$, and $\overline{x} = 320$, we actually achieve reduced error for larger grid spacing as depicted in Figure 2.10b, which is consistent with the poor results noted by Filbet and Laurençot in [43]. Practically speaking, if we wanted to model a system experiencing rapid aggregation and faced limits on gathering data for aggregates with large volume, the FEM would provide more accurate results.

(a) FEM

(b) FLFM

Figure 2.9: Error vs Δx - Grid error at $t = 3$ vs. uniform grid spacing, Δx, when $K(x, y) \equiv 1$, for $\overline{x} = 25$, $\overline{x} = 50$, $\overline{x} = 100$, $\overline{x} = 200$, and $\overline{x} = 400$ in log scale. Clearly, with a slowly aggregating system, grid spacing plays the primary role in accuracy for both methods studied in the paper.

(a) FEM

(b) FLFM

Figure 2.10: Error vs Δx - Grid error at $t = 3$ vs. uniform grid spacing, Δx, when $K(x, y) = xy$, for $\overline{x} = 80$, $\overline{x} = 160$, $\overline{x} = 320$, $\overline{x} = 640$, and $\overline{x} = 1280$ in log scale. For the FEM, grid spacing plays a more important role in accuracy than the truncation parameter, $\overline{x}$, but the FLFM experiences poor behavior when $\overline{x}$ is too small.

2.4 Conclusions and Future Work

The Smoluchowski coagulation equation provides a useful model of particles in suspension in diverse fields of study. Because only a few analytical solutions exist, researchers have developed numerical approaches to approximate solutions to the model. With an eventual goal of comparing simulated solutions with experimental data, we compare two method's accuracies in approximating known and fine grid solutions as well as their accuracies in approximating the zeroth and first moments. We also compare the computation cost of the two methods.

In [2], Ackleh and Fitzpatrick report first order convergence of the FEM in $L^{\infty}[\boldsymbol{X}]$, and in [43], Filbet and Laurençot, report second order convergence of the FLFM in $L^{1}[\boldsymbol{X}]$. Our results support (our conjecture) of second order convergence of the FEM in $L^{1}[\boldsymbol{X}]$ and second order convergence of the FLFM in $L^{1}[\boldsymbol{X}]$, which eliminates any speed advantage the FLFM was previously understood to possess. Furthermore, when approximating a fine grid solution the two methods achieve nearly equal accuracy, with the FLFM achieving slightly higher accuracy for the multiplicative kernel.

Experimental data comes in different forms such as partial zeroth moment distributions or partial first moment distributions. We also theoretically consider the moment approximations and provide numerical evidence that .the FLFM is slightly more accurate approximating the zeroth moment for quickly aggregating systems, and the FEM is much more accurate approximating the zeroth moment when the system aggregates slowly. In terms of approximating the first moment, the FLFM is more accurate for both quickly and slowly aggregating systems.

We also identified discretization resolutions where for the same level of accuracy, the FEM exhibits substantial savings in computational cost over the FLFM For example, the FEM on 800 grid points offers an opportunity of computation cost savings over using the FLFM on 100 grid points while achieving nearly equal accuracy.

We also study the error as a function of both $\overline{x}$ and Δx in an effort to determine the extent to which the truncation parameter, $\overline{x}$, impacts the overall accuracy of the two schemes. Our initial results suggest two important results. The first is not surprising: in general, for the aggregation kernels in this study, reduced grid spacing plays the predominant role in improving numerical accuracy. Second, the FLFM suffers from sensitivity to truncation parameter, $\overline{x}$, when $K(x,y) = xy$, so if experimental data includes a small $\overline{x}$, the FEM should be the method of choice. These intriguing patterns will motivate a more extensive theoretical study of these issue in the future.

Chapter 3

The Inverse Problem

In Chapter 2, with the Smoluchowski coagulation equation as our foundation, we fully compare two numerical schemes in terms of their accuracy in approximating a solution and its zeroth and first moment as well as its computation cost. We conducted that research with the eventual goal of comparing simulated solutions to experimental data. In this chapter, we examine the well-posedness of the inverse problem of parameter estimation. We then take a step towards solving the parameter estimation problem by computing the robustness of our parameter fitting process on artificial data.

As motivation for our work in this chapter, we aim to solve the inverse problem of determining the aggregation kernel in the Smoluchwoski coagulation equation from data provided by Dr. Younger's group. That group would provide data in the form of discrete partial zeroth moment distributions at discrete points in time based on experiments performed on the bacterial pathogen, **Klebsiella pneumoniae**. The measurement devices used in the experiments have minimum and maximum measurement limits. Unfortunately, bacteria can exist in clusters smaller than the lower limit and larger than the upper limit of many measurement devices. With the motivation of identifying the aggregation kernel under real-world experimental limitations, we also aim to rigorously study the impact of the limited measurement domain on our parameter estimation inverse problem.

Before providing parameter estimations, we must mathematically justify our method for solving the proposed inverse problem, for which we model the underlying physical process as an aggregation-only system. As Muraladir explains in [71], when only small clusters exist, an aggregation-only model is reasonable for two reasons. First, in many cases, fragmentation occurs so slowly relative to aggregation. Second, the homogeneity (as defined in (2.4)) of the aggregation kernel permits a study of a strictly small-particle system. Others have provided methods for solving the inverse problem, and Ackleh, Fitzpatrick, and Hallam [3] conduct, to our knowledge, the only rigorous mathematical investigation of the conditions needed to ensure well-posedness. For our numerical method, we rely on the well-posedness results of [20, 35, 36] regarding the forward problem. In Section 3.1, to justify the well-posedness of the inverse problem, we summarize the conditions required, and we outline the major theoretical milestones achieved in [3]. Then in Section 3.2, we provide robustness results for fitting artificial data. Finally in Section 3.3, we describe the future steps necessary to fit our parameter to actual experimental data and determine the impact of limited measurement domains.

3.1 Well-Posedness

To conclude well-posedness for the inverse problem as a whole, we must demonstrate well-posedness for both the forward and inverse problems. Well-posedness for the forward problem requires existence, uniqueness, and continuity of the unique solution on the input parameters. As described in [14] and in [58], well-posedness of the inverse problem requires existence of an optimal aggregation kernel that minimizes the fit, requires method stability, and requires consistency. **Method stability** accounts for two approximations we make when simulating solutions. First, we must approximate the infinite dimensional function space of a allowable aggregation kernels. Second, we must numerically discretize the theoretically continuous volume domain. In both cases, method stability requires convergence of the approximations to their theoretical values. **Consistency** refers to the finite number of observations accompanying any experiment. If our estimate given a finite number of observations converges to the theoretical value given by an infinite number of observations, we consider our estimate consistent. We explain the requirements for well-posedness in more detail in the rest of this section.

The forward problem involves solving the Smoluchowski coagulation equation for the size distribution, f, in (2.2) with a given homogenous aggregation kernel, $K(x, y)$. To reduce notational clutter, where possible, we denote $K(x, y)$ as simply K (we will explicitly specify the cases where K is a constant). Researchers have already established the conditions that allow existence and uniqueness of a solution, f, of the forward problem for the constant, additive, and multiplicative aggregation kernels, $K(x, y) = \gamma$, $K(x, y) = \gamma\,(x + y)$, and $K(x, y) = \gamma\,(xy)$, where $\gamma \in \mathbb{R}_+$ [35, 36]. Furthermore, recall from Chapter 1, we use the superscript, N_x, to indicate a discretized quantity based on a grid with N_x element boundaries. Then, from [20], we know our numerical solutions, f^{N_x}, converge to f as $N_x \to \infty$ for known $K(x,y) \in L^\infty([\underline{x},\overline{x}] \times [\underline{x},\overline{x}])$. In [3], the authors demonstrate convergence of both linear and cubic spline approximations where $K(x,y) \in C([\underline{x},\overline{x}] \times [\underline{x},\overline{x}])$ and $K(x,y) \in C^1([\underline{x},\overline{x}] \times [\underline{x},\overline{x}])$ respectively. To claim well-posedness of the forward problem, we must also prove that the unique solution depends continuously on K, meaning we must prove that $f(t,x;K_i) \to f(t,x;K)$ for any sequence $\{K_i\}_{i=1}^\infty$ where as $i \to \infty$, $K_i \to K$ in $\|\cdot\|_{L^\infty}$ space. In [3], the authors prove continuity of the unique solution in K as inequalities that arise in their existence and uniqueness of solution proofs.

Denoting Ω as the functional space of permissible aggregation kernel functions and following the methodology in [14] and in [58], we intend to demonstrate well-posedness of the inverse problem of determining $K(x,y) \in \Omega$ from experimental zeroth moment distributions. First, the experimentalists provide the total number of bacterial aggregates, $n_{i,k}$, with $i \in [1,M]$ and $k \in [0,N_t]$, possessing a volume in the i^{th} bin across M bins at $N_t + 1$ discrete points, t_k. We denote the edges of the experimental bins $\hat{x}_i$ for $i \in [1, M+1]$, so our data then consists of $N_t + 1$ experimentally determined (observed) zeroth moment distributions, which we denote as

$$\mathbf{n} = \left\{ \{n_{i,k}\}_{i \in [1,M]} \right\}_{k \in [0,N_t]}.$$

We assume the error associated with data observations is log-normal, independent, identically distributed with zero mean and variance σ_n^2. Under that assumption, we describe the observation-model relationship at time t_k and in partition subdomain $[x_i, x_{i+1})$ as being log-normally distributed

$$\log_{10}\{n_{i,k}\} = \log_{10}\{M_0(f(t_k,\cdot);\hat{x}_i,\hat{x}_{i+1})\} + \epsilon;\ \epsilon \in \mathcal{N}(0,\sigma_n^2).$$

Next, we define a cost functional, $C_{N_t}(\mathbf{n},K)$, with $N_t + 1$ observations and $K \in \Omega$ as

$$C_{N_t}(\mathbf{n},K) = \sum_{k=1}^{N_t} \sum_{i=1}^{M} \left\{ \log_{10}\left[M_0(f(t_k,\cdot);\hat{x}_i,\hat{x}_{i+1};K)\right] - \log_{10}\left[n_{i,k}\right] \right\}^2. \tag{3.1}$$

We then define our estimator, K^{N_t}, of the true parameter, K^*, as

$$K^{N_t} = \arg\min_{K \in \Omega} C_{N_t}(\mathbf{n},K) \tag{3.2}$$

and need to prove existence of K^{N_t}.

The next condition for demonstrating well-posedness of the inverse problem requires method stability for the two practical approximations we must make. First, we must approximate the infinite dimensional Ω to some finite dimensional domain, $\Omega_D \subset \Omega$. To specify Ω_D, we need to carefully construct an expanding sequence of partitions, Ω_S, of Ω such that their union, $\Omega_D = \cup_{S=1}^{\infty} \Omega_S$, is dense in Ω. Then by construction, $\exists \left\{ K_{S_j} \right\}_{j=1}^{\infty} \in \Omega_{S_j}$ that converges to K for any $K \in \Omega$. In this approximation space, we actually focus on solving for

$$\begin{aligned} K_S^{N_t} &= \arg \min_{K \in \Omega_S} C_{N_t}(\mathbf{n}, K) \\ &= \arg \min_{K \in \Omega_S} \sum_{k=1}^{N_t} \sum_{i=1}^{M} \left\{ \log_{10} \left[M_0(f(t, \cdot); \hat{x}_i, \hat{x}_{i+1}; K) \right] - \log_{10} \left[n_{i,k} \right] \right\}^2 . \end{aligned}$$

Second, we must demonstrate that our numerical approximation, $M_0^{N_x}(f(t, \cdot); \hat{x}_i, \hat{x}_{i+1}; K)$ is also stable. With this additional approximation, we now solve for

$$\begin{aligned} K_S^{N_t, N_x} &= \arg \min_{K \in \Omega_S} C_{N_t}^{N_x}(\mathbf{n}, K) \\ &= \arg \min_{K \in \Omega_S} \sum_{k=1}^{N_t} \sum_{i=1}^{M} \left\{ \log_{10} \left[M_{0,i}^{N_x}(f(t, \cdot); \hat{x}_i, \hat{x}_{i+1}; K) \right] - \log_{10} \left[n_{i,k} \right] \right\}^2 . \end{aligned}$$

With these two approximations, we must prove that as $N_x, S \to \infty$, $K_S^{N_t, N_x} \to K^{N_t}$.

In Section 3.1 of [3], the authors restate, as Theorem 3.1, the applicable convergence theorem of [14]. They use that theorem to prove existence of a minimizer to (3.2) and to prove stability under approximations of both the permissible function space of allowable aggregation kernels and of the solution space with spline-based collocation schemes. A subtle difference between the set up of the inverse problem in [3] and our inverse problem occurs where we compare approximated zeroth moments to zeroth moment experimental data. Conversely, Ackleh, Fitzpatrick, and Hallam compare approximated size distribution solutions with experimental size distribution data. Despite the subtle difference, the proofs in [3], rely on the assumptions necessary for their numerical methods' respective convergences. In Chapter 2, we prove that convergence of the moment approximation to the analytical moment requires no additional assumptions to those necessary for the numeric convergence of solutions, hence arguments for our formulation of the inverse problem follow similarly to those of [3].

The final condition for well-posedness of the inverse problem requires demonstration of consistency of the estimator, K^{N_t}. If as N_t gets large, K^{N_t} approaches the true K^* in an appropriate way, we say the estimator is consistent. Ackleh, Fitzpatrick, and Hallam do not address this condition in [3].

3.2 Solving the Inverse Problem

Having established the well-posedness requirements in Section 3.1, we next pursue the development of a software implementation for solving the inverse problem. In Section 3.2.1, we describe the process of determining the robustness of our method by fitting artificial data. In Section 3.2.1, we then apply that process to the constant and multiplicative kernels.

3.2.1 Process for fitting artificial data

Our first step toward solving the inverse problem is to use random noise to determine the associated uncertainty in our fit for the constant, γ^{N_t}. In the description that follows, we consider a size independent aggregation kernel, $K^* = \gamma^*$, and explain the process by which we determine an associated uncertainty in our estimate of γ^*. A similar process applies when we fit artificial data for the multiplicative kernel.

Setting $K^* = \gamma^*$, a general solution has the form

$$f(t,x) = \left(\frac{2}{2+\gamma^* t}\right)^2 e^{-\left(\frac{2}{2+\gamma^* t}\right)x}. \tag{3.3}$$

For each of the M experimental bins, and using the solution in (3.3) when $\gamma^* = 2$, we calculate the numerical partial zeroth moments

$$M_0^{N_x}(f(t,\cdot);\hat{x}_i,\hat{x}_{i+1}) = \int_{\hat{x}_i}^{\hat{x}_{i+1}} \left(\frac{2}{2+2t}\right)^2 e^{-\left(\frac{2}{2+2t}\right)x} dy \tag{3.4}$$

for $i \in [1, M]$. Adding noise to (3.4) allows us to establish the robustness of our method by fitting artificial data, which we denote as $\tilde{\mathbf{n}}$. We have included a brief pseudo-code in Listing 3.1 outlining the details of the process.

Listing 3.1: Algorithm to Test Robustness for Method

```
1. define numeric discretization of $N_x - 1$ bins with edges $x_i$ $i \in [1, N_x]$
2. compute initial conditions via assumed $f$ at $t_0$
3. for j=1:(number of noisy samples to fit)
4.         add log-normal random noise to $M_0^{N_x}(f(t,\cdot);\hat{x}_i,\hat{x}_{i+1};\gamma)$ such that
```

```
        $\log_{10}[\tilde{n}_{i,k}] = \log_{10}\left[M_0^{N_x}(f(t,\cdot);\hat{x}_i,\hat{x}_{i+1};\gamma)\right] + \epsilon;\ \ \epsilon \sim \mathcal{N}(0,\sigma^2)$
5.      $\gamma_j^{N_t}$ = minimizer of the $C_{N_t}$ from fitting $\gamma$ ($\gamma_0$ is initial estimate)
6. end
7. compute uncertainty in the estimator $\gamma^{N_t}$ using the set $\{\gamma_j\}$
```

3.2.2 Results from fitting artificial data

To execute the algorithm in Listing 3.1, we implement a *trust-region-reflective* optimization via Matlab's **lsqnonlin**, and we generate the robustness results depicted in Figures 3.1 and 3.2 for the constant and multiplicative kernels. To approximate an experimental domain, we set $[x_1, x_{M+1}] = [0.001, 25]$ for the constant kernel and $[x_1, x_{M+1}] = [0.75, 700]$ for the multiplicative kernel. For both kernels, we set $[t_1, t_{N_t}] = [1, 3]$, $N_t = 8$, and $M = 4$, and we run our numerical simulation on the same domain, but with a fine volume grid, where $N_x = 200$. Also for both kernels, we start with an initial estimate of $\gamma_0 = 4$. For each kernel we fit $\gamma_j^{N_t}$ 100 times for each of five levels of simulated measurement noise with standard deviation, σ_n. From each of those 100 fits, we compute the mean, which we denote $\overline{\gamma^{N_t}}(\sigma_n)$,

$$\overline{\gamma^{N_t}}(\sigma_n) = \frac{\sum_{j=1}^{100} \gamma_j^{N_t}}{100},$$

and the variation which we denote as $\sigma^2_{\gamma_j^{N_t}}(\sigma_n)$,

$$\sigma^2_{\gamma_j^{N_t}}(\sigma_n) = \frac{1}{100}\sum_{j=1}^{100}\left[\gamma_j^{N_t}(\sigma_n) - \overline{\gamma^{N_t}}(\sigma_n)\right]^2.$$

In Figure 3.1, we observe an increase in the variability of $\gamma_j^{N_t}(\sigma_n)$ as we increase the simulated measurement noise.

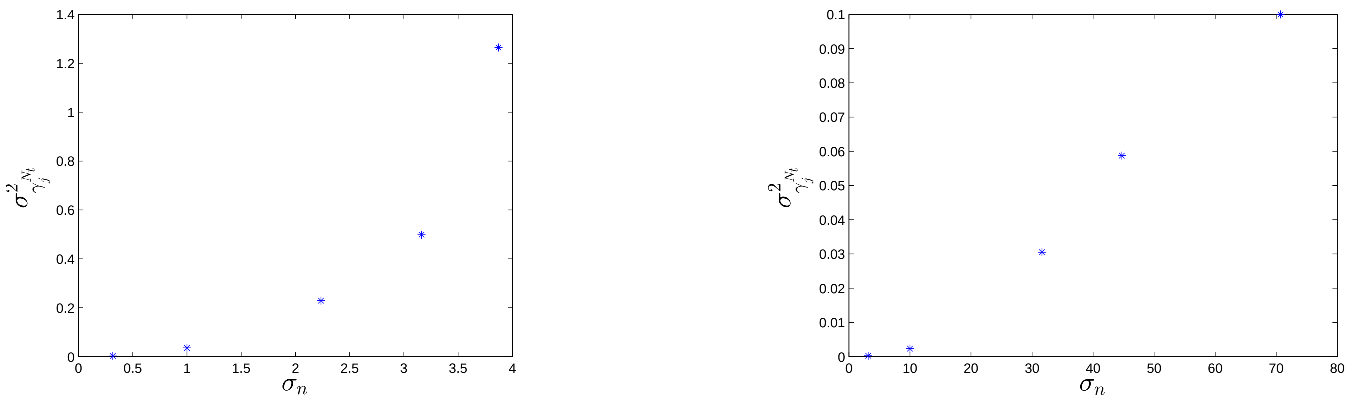

(a) Constant kernel with $\gamma^* = 2$

(b) Multiplicative kernel with $\gamma^* = 2$

Figure 3.1: Variation in the parameter estimate vs. change in the level of simulated measurement noise: for both the constant and multiplicative kernels, the variation in the parameter estimate increases with an increase in simulated measurement noise.

Similarly, Figure 3.2 depicts an increase in measurement noise producing an increase in the error, defined simply as $\left|\gamma^* - \overline{\gamma^{N_t}}(\sigma_n)\right|$. Note that we produce less error in the parameter estimate for the multiplicative kernel even with greater measurement noise levels, but we expect this due to the much larger range of comparison volumes.

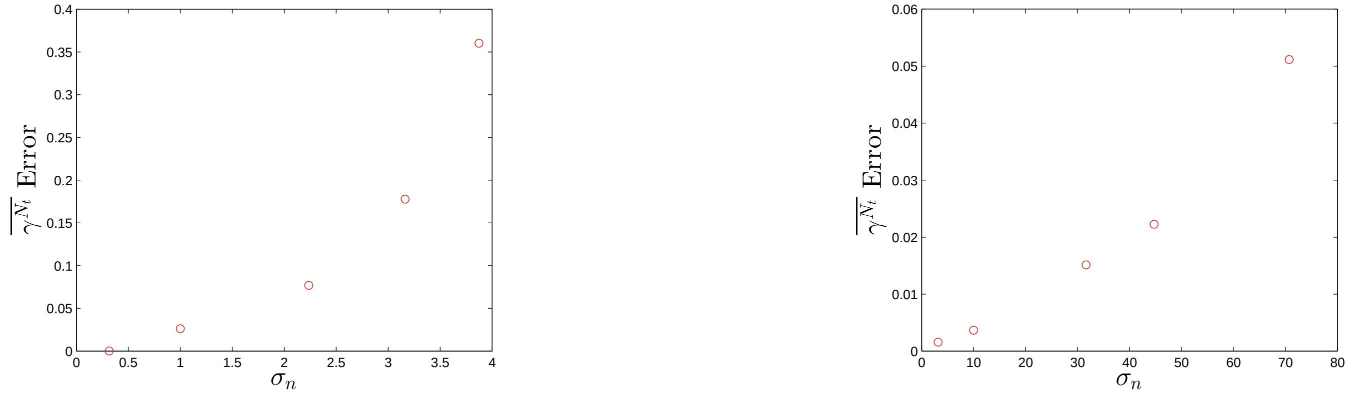

(a) Constant kernel with $\gamma^* = 2$

(b) Multiplicative kernel with $\gamma^* = 2$

Figure 3.2: Error in the parameter estimate, $\left|\gamma^* - \overline{\gamma^{N_t}}(\sigma_n)\right|$, vs. change in the level of simulated measurement noise: for both the constant and multiplicative kernels, the error in the parameter estimate increases with an increase in simulated measurement noise.

3.3 Future Work

Parameter estimation from experimental data motivates our work in this chapter. In the future, to reach this goal, have two specific areas we want to study. First, we describe in Section 3.3.1 the process by which we will actually perform the parameter estimation from experimental data. Second, we discuss in Section 3.3.2 the manner in which we intend to fully explore the impacts to the accuracy of our estimations when we lack data.

3.3.1 Fitting experimental data

With our robustness results of our fitting procedure for each of the aforementioned aggregation kernels complete, we have the tools necessary to estimate γ^* using experimental data. We will first assume that the original biomass has fragmented in many small clusters (where the limiting distribution would consist solely of individual bacteria cells), and we will use the assumed form of f at t_0, for each respective kernel, to determine the initial conditions from a 1-D fit for γ_0 at t_0. We will then solve the PDE forward for the remaining t_k. Using that set of solutions, we will determine the numerical zeroth moments across the M experimental bins and will fit for γ^{N_t} against the experimental data where the fit procedure minimizes the cost function in (3.1).

3.3.2 Estimates in the absence of full data

The final portion of our future work will fully explore the accuracy of our estimation of γ^* in the absence of full data. Using similar steps to those in Section 3.3.1, we will iterate our fit against experimental data for expanding subsets of the original M bins. With each successive expansion of bins used, we will examine the rate of change in the error. Assuming similarity exists physically, we expect the optimal data range to occur where the largest ratio, $\overline{x}/\underline{x}$, occurs. Finally, we will compare the results across multiple aggregation kernels.

Chapter 4

Generalized sensitivity functions for sized structured population models

General structured population models provide a link from the individuals in a population to the population processes [37, 38, 85]. Size-structured population models, which describe the distribution of of individuals throughout varying size classes, have increased in popularity over the past several years [23, 30]. Typical ODE based population models make a number of simplifying assumptions, a major one of which presumes homogeneity of the population's physical structure. One effort to relax the homogeneity assumption resulted in the creation of age-structured population models which account for the effects of differing ages amongst the individuals comprising the population. Unfortunately, for many systems, age does not comprise the most influential physical attribute [24], which necessitated the development of size-structured population models.

Parameter estimation based on experimental data (an inverse problem) provides a natural context to which we can apply size-structured population models. With a goal of optimizing the experiments, we seek to sample from domains which contain the most relevant information regarding the parameter estimation. Generalized sensitivity functions provide a tool which quantifies the importance of specific regions of a domain to the parameter of interest. Previous studies, such as cardiovascular regulation [16, 44, 45], HIV modeling [27], and HTLV-1 transactivation simulation [22], have applied the generalized sensitivity functions to ordinary differential equations. We denote these ODE-based GSFs as OGSFs. With our emphasis on size-structured population models, the primary goal of our work in this chapter is to extend the concepts of OGSFs to the application of generalized sensitivity functions to PDEs, which we denote as PGSFs.

Thomaseth and Cobelli introduced the concept of OGSFs in [84][1] and Batzel et al. recast the OGSFs

---

[1] Note that in the original Thomaseth and Cobelli work, the functions are simply called GSFs (not OGSFs), since the authors are only considering ODE-based models.

into a probabilistic setting [17]. In a series of studies, Banks et al. [9–11] further develop the OGSF concept.. In particular, the work by Banks, Dediu, and Ernstberger [10] compares traditional sensitivity functions (TSFs) with OGSFs (in the context of general nonlinear ODEs) and highlights the potential utilities of OGSFs. In [10], the authors also warn that OGSFs possess a potential weakness, which they denote as the **forced-to-one artifact** (discussed in Section 4.1). Then Banks, Davidian, Samuels, and Sutton [9] expand the results in [10] by introducing methodology for choosing between TSFs and OGSFs. Later, Banks, Dediu, Ernstberger, and Kappel [11] extend the OGSFs to a continuous setting and demonstrate the value of the OGSFs in the context of optimal experimental design.

As a case study for our extension of OGSFs to the PDE context, we apply our PGSFs to the Smoluchowski coagulation equation. This model for size-structured populations arises in the study of organic phenomena such as bacterial growth [20], marine snow [48], algal blooms [1, 2, 79], and schooling fish [72] and inorganic phenomena such as powder metallurgy [51], astronomy [56, 57, 65, 81], aerosols [34], irradiation of metals [83], and meteorology [76]. For our study, we determine the time and volume subdomains, which we denote $\mathcal{D}^*$, of greatest relevance to the estimate of the constant parameter in three coagulation kernels. In Section 4.1, we summarize the original work on OGSFs and the extensions to it. We then make a further extention of OGSFs to PGSFs for implementation on size-structured population models. In Section 4.2, we discuss the details of how we implement the PGSFs with respect to the Smoluchowski coagulation equation. In Section 4.3, we provide our results for each of three coagulation kernels. Finally in Section 4.4, we summarize the conclusions we have drawn from this study and discuss future directions for this research.

4.1 Generalized sensitivity functions Theory

Given a domain $\mathcal{D}$ for the independent variables, the PGSFs will allow us to identify a subregion $\mathcal{D}^* \subset \mathcal{D}$, containing the information necessary to make the most accurate parameter estimates. The OGSFs and PGSFs vary from the TSFs[2] in the sense that the OGSFs and PGSFs do not depend on specific data realizations, which we explain in more detail in Section 4.1.1. When Thomaseth and Cobelli introduced the OGSFs in [84], they argued that the subdomain over which the OGSFs most rapidly increase to one contains

---

[2] For a summary of TSFs, see Stanley and Stewart [82].

the most relevant information for the parameter of interest. Then in [11], Banks et al. provide evidence that subdomains over which the OGSFs most rapidly decrease (indicating a high correlation between multiple parameters) also contain high information content.

In addition to the OGSFs, Thomaseth and Cobelli provide a related tool, the incremental (O)GSF, which computes the information at a given time point informing the value of a parameter estimate [84]. As advocated by the authors, the OGSFs and the incremental OGSFs should be regarded as complementary to one another. To demonstrate the complementary characteristics of OGSFs and incremental OGSFs, Thomaseth and Cobelli present an example where the plots of the OGSFs suggest an optimal $\mathcal{D}^*$. Banks et al. define a related quantity, the time derivative of the OGSFs, which plays the role of an incremental GSF when the OGSF is defined over continuous time (see a similarly complementary role to the continuous OGSFs.

As mentioned above, one weakness of generalized sensitivity functions is the so called **forced to one artifact** (FTOA). As addressed at length by Banks, Dediu, and Enrstberger in [10], plots of the OGSFs vary with changes in $\mathcal{D}$. Regardless of the choice of domain, by definition, the OGSFs and PGSFs will attain a value of one at the independent variables' maximum values in $\mathcal{D}$. Therefore, if $\mathcal{D}$ possesses insufficient maximum values, the generalized sensitivity functions may provide misleading information about $\mathcal{D}^*$ because they were (by definition) forced to a value of one on the upper bound of the domain. A strategy to counter this weakness [11] is to check that the time derivative of the OGSFs approaches zero within the original choice of $\mathcal{D}$. If it does not, we extend $\mathcal{D}$ until the derivative does satisfy this criteria.

In Section 4.1.1, we summarize Thomaseth's and Cobelli's and Banks et al.'s development of the discrete and continuous OGSFs, respectively. In Section 4.1.3, we extend these previous works to the continuous PGSFs setting necessary for parameter estimation in size-structured population, PDE models. Finally, in Section 4.1.4, we propose mathematical criteria for determining $\mathcal{D}^*$.

4.1.1 ODE-Based GSFs (OGSFs)

In this section, we summarize the theory introduced by Thomaseth and Cobelli in [84], and the analysis needed for (4.1) through (4.15) follows directly from that work. First, we represent the system under consideration as a nonlinear regression function $f(t;\theta)$ with t representing the sole independent variable and with $\boldsymbol{\theta} = [\theta_1, \theta_2, \ldots, \theta_L]^T$ representing the parameter column vector with dimension L.[3] Then we represent the measurements with noise as

$$y(t_k) = f(t_k; \boldsymbol{\theta}) + \epsilon(t),\ k = 1, \ldots, N_t \tag{4.1}$$

where $\epsilon(t_k)$ is the measurement noise. We assume an independent identically distributed noise distribution with zero mean and with known (but possibly time varying) variance, $\sigma^2(t_k)$. We also assume the existence of a true parameter vector $\boldsymbol{\theta}_0$ which generates realizations $y(t_k)$ in (4.1).

To provide extra details for certain concepts as we progress, we let $\dim \boldsymbol{\theta} = 2$ with the column vector $\boldsymbol{\theta} = [\theta_1, \theta_2]^T$, and we let $N_t = 3$. With traditional sensitivity analysis, we consider the time evolution of changes in $f(t; \boldsymbol{\theta})$ with respect to the parameters. We denote this evolution with a column vector $\nabla_{\boldsymbol{\theta}} f(t; \boldsymbol{\theta})$. We then model the changes in the output evolution with respect to small perturbations of the model parameters with

$$\delta y(t_k) = \nabla_{\boldsymbol{\theta}} f(t; \boldsymbol{\theta})^T \delta \boldsymbol{\theta} = \begin{bmatrix} \frac{\partial f(t_k;\boldsymbol{\theta})}{\partial \theta_1} & \frac{\partial f(t_k;\boldsymbol{\theta})}{\partial \theta_2} \end{bmatrix} \begin{bmatrix} \delta\theta_1 \\ \delta\theta_2 \end{bmatrix} = \frac{\partial f(t_k; \boldsymbol{\theta})}{\partial \theta_1} \delta\theta_1 + \frac{\partial f(t_k; \boldsymbol{\theta})}{\partial \theta_2} \delta\theta_2. \tag{4.2}$$

The TSFs then develop as presented in [84], but as Thomaseth and Cobelli warn, the TSFs do not account for how sensitive the estimates of model parameters are to the true parameters. As a means of quantifying the relevance of specific subregions of $\mathcal{D}$ on parameter estimates, Thomaseth and Cobelli introduce the OGSFs by first denoting the column vector of observations as $\boldsymbol{y} = [y(t_1), y(t_2), \ldots, y(t_{N_t})]^T$. We then estimate $\boldsymbol{\theta}_0$ in the time domain by minimizing the weighted residual sum of squares (WRSS) where

$$WRSS(\boldsymbol{y}; \boldsymbol{\theta}) = \sum_{i=1}^{N_t} \frac{[y(t_i) - f(t_i; \boldsymbol{\theta})]^2}{\sigma^2(t_i)}. \tag{4.3}$$

The nonlinear WLS estimate is

$$\hat{\boldsymbol{\theta}} = \arg \min_{\boldsymbol{\theta}} WRSS(\boldsymbol{y}; \boldsymbol{\theta}) \tag{4.4}$$

---

[3] Note that bold typeface indicates a vector quantity.

that satisfies

$$\begin{aligned}
\mathbf{0} &= \nabla_{\boldsymbol{\theta}} WRSS(\boldsymbol{y};\boldsymbol{\theta})\,\big|_{\boldsymbol{\theta}=\hat{\boldsymbol{\theta}}} \equiv \nabla_{\boldsymbol{\theta}} WRSS(\boldsymbol{y};\hat{\boldsymbol{\theta}}) \\
&= \begin{bmatrix} \frac{\partial}{\partial\theta_1} WRSS(\boldsymbol{y};\boldsymbol{\theta}) \\ \frac{\partial}{\partial\theta_2} WRSS(\boldsymbol{y};\boldsymbol{\theta}) \end{bmatrix}\Bigg|_{\boldsymbol{\theta}=\hat{\boldsymbol{\theta}}} \\
&= \begin{bmatrix} -2\sum_{i=1}^{N_t=3} \frac{[y(t_i)-f(t_i;\boldsymbol{\theta})]}{\sigma^2(t_i)} \frac{\partial f(t_i;\boldsymbol{\theta})}{\partial\theta_1} \\ -2\sum_{i=1}^{N_t=3} \frac{[y(t_i)-f(t_i;\boldsymbol{\theta})]}{\sigma^2(t_i)} \frac{\partial f(t_i;\boldsymbol{\theta})}{\partial\theta_2} \end{bmatrix}\Bigg|_{\boldsymbol{\theta}=\hat{\boldsymbol{\theta}}}. \qquad (4.5)
\end{aligned}$$

Furthermore, Thomaseth and Cobelli assume that the parameter estimates, $\hat{\boldsymbol{\theta}}$, are unbiased, i.e., $E[\hat{\boldsymbol{\theta}}] = \boldsymbol{\theta}_0$.

At this point in the derivation of OGSFs, Thomaseth and Cobelli aim to remove explicit dependence on the data observations. They define the variation of model outputs with a small variation $\delta\boldsymbol{\theta}_0$ of the true parameters as

$$\begin{aligned}
\delta\boldsymbol{y} &= \begin{bmatrix} \nabla_{\boldsymbol{\theta}} f(t_1;\boldsymbol{\theta}_0)^T \\ \nabla_{\boldsymbol{\theta}} f(t_2;\boldsymbol{\theta}_0)^T \\ \nabla_{\boldsymbol{\theta}} f(t_3;\boldsymbol{\theta}_0)^T \end{bmatrix} \delta\boldsymbol{\theta}_0 \\
&= \begin{bmatrix} \frac{\partial f(t_1;\boldsymbol{\theta}_0)}{\partial\theta_1} & \frac{\partial f(t_1;\boldsymbol{\theta}_0)}{\partial\theta_2} \\ \frac{\partial f(t_2;\boldsymbol{\theta}_0)}{\partial\theta_1} & \frac{\partial f(t_2;\boldsymbol{\theta}_0)}{\partial\theta_2} \\ \frac{\partial f(t_3;\boldsymbol{\theta}_0)}{\partial\theta_1} & \frac{\partial f(t_3;\boldsymbol{\theta}_0)}{\partial\theta_2} \end{bmatrix} \begin{bmatrix} \delta\theta_{0,1} \\ \delta\theta_{0,2} \end{bmatrix} \qquad (4.6) \\
&= \begin{bmatrix} \frac{\partial f(t_1;\boldsymbol{\theta}_0)}{\partial\theta_1}\delta\theta_{0,1} + \frac{\partial f(t_1;\boldsymbol{\theta}_0)}{\partial\theta_2}\delta\theta_{0,2} \\ \frac{\partial f(t_2;\boldsymbol{\theta}_0)}{\partial\theta_1}\delta\theta_{0,1} + \frac{\partial f(t_2;\boldsymbol{\theta}_0)}{\partial\theta_2}\delta\theta_{0,2} \\ \frac{\partial f(t_3;\boldsymbol{\theta}_0)}{\partial\theta_1}\delta\theta_{0,1} + \frac{\partial f(t_3;\boldsymbol{\theta}_0)}{\partial\theta_2}\delta\theta_{0,2} \end{bmatrix}. \qquad (4.7)
\end{aligned}$$

By making the assumption that the outputs vary independently of measurement error, $\delta\boldsymbol{y}$ causes $\delta\hat{\boldsymbol{\theta}}$ in a manner where (4.5) still holds, which implies

$$\mathbf{0} \approx \nabla_{\boldsymbol{\theta}} WRSS(\boldsymbol{y}+\delta\boldsymbol{y};\hat{\boldsymbol{\theta}}+\delta\hat{\boldsymbol{\theta}}).$$

We then make a first order Taylor approximation around $(\boldsymbol{y};\hat{\boldsymbol{\theta}})$ such that

$$\begin{aligned}
\mathbf{0} &\approx \nabla_{\boldsymbol{\theta}} WRSS(\boldsymbol{y};\hat{\boldsymbol{\theta}}) + \nabla^2_{\boldsymbol{\theta}\boldsymbol{\theta}} WRSS(\boldsymbol{y};\hat{\boldsymbol{\theta}})\delta\hat{\boldsymbol{\theta}} + \nabla^2_{\boldsymbol{\theta}\boldsymbol{y}} WRSS(\boldsymbol{y};\hat{\boldsymbol{\theta}})\delta\boldsymbol{y} \\
&= \nabla^2_{\boldsymbol{\theta}\boldsymbol{\theta}} WRSS(\boldsymbol{y};\hat{\boldsymbol{\theta}})\delta\hat{\boldsymbol{\theta}} + \nabla^2_{\boldsymbol{\theta}\boldsymbol{y}} WRSS(\boldsymbol{y};\hat{\boldsymbol{\theta}})\delta\boldsymbol{y}, \qquad (4.8)
\end{aligned}$$

where $\nabla^2_{\boldsymbol{\theta\theta}}$ and $\nabla^2_{\boldsymbol{\theta y}}$ denote second order derivatives. By inverting the matrix, $\nabla^2_{\boldsymbol{\theta\theta}} WRSS(\boldsymbol{y};\hat{\boldsymbol{\theta}})$ (2x2 in our example), we can solve (4.8) for $\delta\hat{\boldsymbol{\theta}}$ whereby

$$\delta\hat{\boldsymbol{\theta}} \approx -\left[\nabla^2_{\boldsymbol{\theta\theta}} WRSS(\boldsymbol{y};\hat{\boldsymbol{\theta}})\right]^{-1} \nabla^2_{\boldsymbol{\theta y}} WRSS(\boldsymbol{y};\hat{\boldsymbol{\theta}})\delta\boldsymbol{y}. \tag{4.9}$$

Notice $\delta\hat{\boldsymbol{\theta}}$ depends on $\boldsymbol{y}$ and $\delta\boldsymbol{y}$ in (4.9). We now apply the chain rule to (4.8) to compute

$$\begin{aligned}
\nabla^2_{\boldsymbol{\theta\theta}} WRSS(\boldsymbol{y};\hat{\boldsymbol{\theta}}) &= \nabla_{\boldsymbol{\theta}}\left(\nabla_{\boldsymbol{\theta}} WRSS(\boldsymbol{y};\boldsymbol{\theta})\right) \\
&= \nabla_{\boldsymbol{\theta}}\left(\begin{bmatrix} -2\sum_{i=1}^{N_t=3} \frac{[y(t_i)-f(t_i;\boldsymbol{\theta})]}{\sigma^2(t_i)} \frac{\partial f(t_i;\boldsymbol{\theta})}{\partial\theta_1} \\ -2\sum_{i=1}^{N_t=3} \frac{[y(t_i)-f(t_i;\boldsymbol{\theta})]}{\sigma^2(t_i)} \frac{\partial f(t_i;\boldsymbol{\theta})}{\partial\theta_2} \end{bmatrix}\right) \\
&= 2\sum_{i=1}^{N_t=3} \begin{bmatrix} \frac{\frac{\partial f(t_i;\boldsymbol{\theta})}{\partial\theta_1}}{\sigma^2(t_i)} \frac{\partial f(t_i;\boldsymbol{\theta})}{\partial\theta_1} & \frac{\frac{\partial f(t_i;\boldsymbol{\theta})}{\partial\theta_2}}{\sigma^2(t_i)} \frac{\partial f(t_i;\boldsymbol{\theta})}{\partial\theta_1} \\ \frac{\frac{\partial f(t_i;\boldsymbol{\theta})}{\partial\theta_1}}{\sigma^2(t_i)} \frac{\partial f(t_i;\boldsymbol{\theta})}{\partial\theta_2} & \frac{\frac{\partial f(t_i;\boldsymbol{\theta})}{\partial\theta_2}}{\sigma^2(t_i)} \frac{\partial f(t_i;\boldsymbol{\theta})}{\partial\theta_2} \end{bmatrix} \\
&- 2\sum_{i=1}^{N_t=3} \begin{bmatrix} \frac{[y(t_i)-f(t_i;\boldsymbol{\theta})]}{\sigma^2(t_i)} \frac{\partial^2 f(t_i;\boldsymbol{\theta})}{\partial\theta_1^2} & \frac{[y(t_i)-f(t_i;\boldsymbol{\theta})]}{\sigma^2(t_i)} \frac{\partial^2 f(t_i;\boldsymbol{\theta})}{\partial\theta_1\partial\theta_2} \\ \frac{[y(t_i)-f(t_i;\boldsymbol{\theta})]}{\sigma^2(t_i)} \frac{\partial^2 f(t_i;\boldsymbol{\theta})}{\partial\theta_2\partial\theta_1} & \frac{[y(t_i)-f(t_i;\boldsymbol{\theta})]}{\sigma^2(t_i)} \frac{\partial^2 f(t_i;\boldsymbol{\theta})}{\partial\theta_2^2} \end{bmatrix} \\
&= \sum_{i=1}^{N_t=3} \frac{2}{\sigma^2(t_i)} \left[\nabla_{\boldsymbol{\theta}} f(t_i;\boldsymbol{\theta}) \nabla_{\boldsymbol{\theta}} f(t_i;\boldsymbol{\theta})^T\right] \\
&- \sum_{i=1}^{N_t=3} \frac{2}{\sigma^2(t_i)} \left\{\left[y(t_i)-f(t_i;\boldsymbol{\theta})\right] \nabla^2_{\boldsymbol{\theta\theta}} f(t_i;\boldsymbol{\theta})\right\}
\end{aligned} \tag{4.10}$$

Next we note

$$\frac{d\nabla_{\boldsymbol{\theta}} WRSS(\boldsymbol{y};\boldsymbol{\theta})}{dy(t_i)} = -\frac{2}{\sigma^2(t_i)} \nabla_{\boldsymbol{\theta}} f(t_i;\boldsymbol{\theta})$$

and apply the chain rule to (4.8) again to compute

$$\begin{aligned}
\nabla^2_{\boldsymbol{\theta y}} WRSS(\boldsymbol{y};\hat{\boldsymbol{\theta}}) &= \begin{bmatrix} -\frac{2}{\sigma^2(t_1)}\nabla_{\boldsymbol{\theta}} f(t_1;\boldsymbol{\theta}) & -\frac{2}{\sigma^2(t_2)}\nabla_{\boldsymbol{\theta}} f(t_2;\boldsymbol{\theta}) & -\frac{2}{\sigma^2(t_3)}\nabla_{\boldsymbol{\theta}} f(t_3;\boldsymbol{\theta}) \end{bmatrix} \\
&= \begin{bmatrix} -\frac{2}{\sigma^2(t_1)} \frac{\partial f(t_1;\boldsymbol{\theta})}{\partial\theta_1} & -\frac{2}{\sigma^2(t_2)} \frac{\partial f(t_2;\boldsymbol{\theta})}{\partial\theta_1} & -\frac{2}{\sigma^2(t_3)} \frac{\partial f(t_3;\boldsymbol{\theta})}{\partial\theta_1} \\ -\frac{2}{\sigma^2(t_1)} \frac{\partial f(t_1;\boldsymbol{\theta})}{\partial\theta_2} & -\frac{2}{\sigma^2(t_2)} \frac{\partial f(t_2;\boldsymbol{\theta})}{\partial\theta_2} & -\frac{2}{\sigma^2(t_3)} \frac{\partial f(t_3;\boldsymbol{\theta})}{\partial\theta_2} \end{bmatrix}.
\end{aligned} \tag{4.11}$$

To remove the dependence on $\boldsymbol{y}$ and $\delta\boldsymbol{y}$ in (4.9), we substitute the **a priori** expected values of the matrices in (4.9) resulting in

$$\begin{aligned}
E\left[\nabla^2_{\boldsymbol{\theta\theta}} WRSS(\boldsymbol{y},\hat{\boldsymbol{\theta}})\right] &= \nabla^2_{\boldsymbol{\theta\theta}} WRSS(\boldsymbol{y};\hat{\boldsymbol{\theta}})\Big|_{\hat{\boldsymbol{\theta}}=\boldsymbol{\theta}_0} \\
&= 2\left[\sum_{i=1}^{N_t=3} \frac{1}{\sigma^2(t_i)} \nabla_{\boldsymbol{\theta}} f(t_i;\boldsymbol{\theta}_0) \nabla_{\boldsymbol{\theta}} f(t_i;\boldsymbol{\theta}_0)^T - \sum_{i=1}^{N_t=3} \frac{[y(t_i)-f(t_i;\boldsymbol{\theta}_0)]}{\sigma^2(t_i)} \nabla^2_{\boldsymbol{\theta\theta}} f(t_i;\boldsymbol{\theta}_0)\right] \\
&= 2\sum_{i=1}^{N_t=3} \frac{1}{\sigma^2(t_i)} \nabla_{\boldsymbol{\theta}} f(t_i;\boldsymbol{\theta}_0) \nabla_{\boldsymbol{\theta}} f(t_i;\boldsymbol{\theta}_0)^T.
\end{aligned} \tag{4.12}$$

The second sum vanishes when we note that by our earlier assumption, $y(t_i) = f(t_i; \boldsymbol{\theta}_0)$. Furthermore,

$$\begin{aligned} E\left[\nabla^2_{\boldsymbol{\theta y}} WRSS(\boldsymbol{y}; \hat{\boldsymbol{\theta}})\right] &= \nabla^2_{\boldsymbol{\theta y}} WRSS(\boldsymbol{y}; \hat{\boldsymbol{\theta}})\Big|_{\hat{\boldsymbol{\theta}}=\boldsymbol{\theta}_0} \\ &= -2\begin{bmatrix} \frac{\nabla_{\boldsymbol{\theta}} f(t_1;\boldsymbol{\theta}_0)}{\sigma^2(t_1)} & \frac{\nabla_{\boldsymbol{\theta}} f(t_2;\boldsymbol{\theta}_0)}{\sigma^2(t_2)} & \frac{\nabla_{\boldsymbol{\theta}} f(t_3;\boldsymbol{\theta}_0)}{\sigma^2(t_3)} \end{bmatrix}. \end{aligned} \tag{4.13}$$

We then substitute (4.6), (4.12), and (4.13) into (4.9) to derive

$$\begin{aligned} \delta\hat{\boldsymbol{\theta}} &\approx \left[\sum_{i=1}^{N_t=3} \frac{1}{\sigma^2(t_i)} \nabla_{\boldsymbol{\theta}} f(t_i; \boldsymbol{\theta}_0) \nabla_{\boldsymbol{\theta}} f(t_i; \boldsymbol{\theta}_0)^T\right]^{-1} \\ &\times \begin{bmatrix} \frac{\nabla_{\boldsymbol{\theta}} f(t_1;\boldsymbol{\theta}_0)}{\sigma^2(t_1)} & \frac{\nabla_{\boldsymbol{\theta}} f(t_2;\boldsymbol{\theta}_0)}{\sigma^2(t_2)} & \frac{\nabla_{\boldsymbol{\theta}} f(t_3;\boldsymbol{\theta}_0)}{\sigma^2(t_3)} \end{bmatrix} \begin{bmatrix} \frac{\partial f(t_1;\boldsymbol{\theta}_0)}{\partial\theta_1} & \frac{\partial f(t_1;\boldsymbol{\theta}_0)}{\partial\theta_2} \\ \frac{\partial f(t_2;\boldsymbol{\theta}_0)}{\partial\theta_1} & \frac{\partial f(t_2;\boldsymbol{\theta}_0)}{\partial\theta_2} \\ \frac{\partial f(t_3;\boldsymbol{\theta}_0)}{\partial\theta_1} & \frac{\partial f(t_3;\boldsymbol{\theta}_0)}{\partial\theta_2} \end{bmatrix} \begin{bmatrix} \delta\theta_{0,1} \\ \delta\theta_{0,2} \end{bmatrix} \\ &= \left[\sum_{i=1}^{N_t=3} \frac{1}{\sigma^2(t_i)} \nabla_{\boldsymbol{\theta}} f(t_i; \boldsymbol{\theta}_0) \nabla_{\boldsymbol{\theta}} f(t_i; \boldsymbol{\theta}_0)^T\right]^{-1} \sum_{i=1}^{3} \begin{bmatrix} \frac{\frac{\partial^2 f}{\partial\theta_1^2}(t_i;\boldsymbol{\theta}_0)}{\sigma^2(t_i)} & \frac{\frac{\partial^2 f}{\partial\theta_1\partial\theta_2}(t_i;\boldsymbol{\theta}_0)}{\sigma^2(t_i)} \\ \frac{\frac{\partial^2 f}{\partial\theta_2\partial\theta_1}(t_i;\boldsymbol{\theta}_0)}{\sigma^2(t_i)} & \frac{\frac{\partial^2 f}{\partial\theta_1^2}(t_i;\boldsymbol{\theta}_0)}{\sigma^2(t_i)} \end{bmatrix} \delta\boldsymbol{\theta}_0 \\ &= \left[\sum_{i=1}^{N_t=3} \frac{1}{\sigma^2(t_i)} \nabla_{\boldsymbol{\theta}} f(t_i; \boldsymbol{\theta}_0) \nabla_{\boldsymbol{\theta}} f(t_i; \boldsymbol{\theta}_0)^T\right]^{-1} \left[\sum_{i=1}^{3} \frac{1}{\sigma^2(t_i)} \nabla_{\boldsymbol{\theta}} f(t_i; \boldsymbol{\theta}_0) \nabla_{\boldsymbol{\theta}} f(t_i; \boldsymbol{\theta}_0)^T\right] \delta\boldsymbol{\theta}_0 \\ &= \mathbf{I}\delta\boldsymbol{\theta}_0 \end{aligned} \tag{4.14}$$

The result in (4.14) generates two important considerations. First, (4.14) preserves the assumption of unbiased parameter estimates. Second, the vanishing of off-diagonal elements implies that we can estimate variations of the true parameters independently of one another. When the observation times are discrete (as in [84]), the generalized sensitivity is defined as

$$\boldsymbol{gs}(t_k) = \sum_{i=1}^{k} \left\{ \left(\left[\sum_{j=1}^{N_t} \frac{1}{\sigma^2(t_j)} \nabla_{\boldsymbol{\theta}} f(t_j; \boldsymbol{\theta}_0) \nabla_{\boldsymbol{\theta}} f(t_j; \boldsymbol{\theta}_0)^T\right]^{-1} \frac{\nabla_{\boldsymbol{\theta}} f(t_i; \boldsymbol{\theta}_0)}{\sigma^2(t_i)} \right) \bullet \nabla_{\boldsymbol{\theta}} f(t_i; \boldsymbol{\theta}_0) \right\}, \tag{4.15}$$

where $\bullet$ indicates a Hadamard product. The authors assert that the Hadamard product enforces including only the diagonal elements in the matrix operations in (4.14).

In the appendix to [84], the authors also introduce the incremental OGSFs defined as

$$\boldsymbol{gs}_{inc}(t_k) = \boldsymbol{gs}(t_k) - \boldsymbol{gs}(t_{k-1}),$$

yielding

$$\boldsymbol{gs}_{inc}(t_k) = \left(\left[\sum_{j=1}^{N_t} \frac{1}{\sigma^2(t_j)} \nabla_{\boldsymbol{\theta}} f(t_j; \boldsymbol{\theta}_0) \nabla_{\boldsymbol{\theta}} f(t_j; \boldsymbol{\theta}_0)^T \right]^{-1} \frac{\nabla_{\boldsymbol{\theta}} f(t_k; \boldsymbol{\theta}_0)}{\sigma^2(t_k)} \right) \bullet \nabla_{\boldsymbol{\theta}} f(t_k; \boldsymbol{\theta}_0). \tag{4.16}$$

With this definition (4.16), one can calculate the contribution of the partial derivative at a specific point, t_k, rather than sum all contributions at times up to and including t_k.

4.1.2 Continuous OGSFs

In this section, we summarize the work in [11], where Banks et al. develop a continuous version of the generalized sensitivity functions, and we highlight connections between their work and that of Thomaseth and Cobelli [84]. Analogous to the discrete weighted residual sum of squares (WRSS) in (4.3), Banks et al. define the error functional

$$C(y; \boldsymbol{\theta}) = \int_0^{\bar{t}} \frac{1}{\sigma^2(t)} \left(y(t) - f(t; \boldsymbol{\theta}) \right)^2 dP(t) \tag{4.17}$$

where P is a general measure on $[0, \bar{t}]$. Without loss of generality, the authors also assume P is a probability measure on $[0, \bar{t}]$. They then assume that $C(y; \boldsymbol{\theta})$ is differentiable with respect to $\boldsymbol{\theta}$ and derive the analogous optimality condition

$$\int_0^{\bar{t}} \frac{1}{\sigma^2(t)} \left(y(s; \boldsymbol{\theta}_0) - f(s; \hat{\boldsymbol{\theta}}) \right) \nabla_{\boldsymbol{\theta}} f(s; \hat{\boldsymbol{\theta}}) dP(s) = 0. \tag{4.18}$$

With reasoning similar to that of Thomaseth and Cobelli, Banks et al. then assume unbiased parameter estimates and consider appropriate expected values to derive functions independent of realizations. They then argue that they can approximate the expected value of $\nabla^2_{\boldsymbol{\theta}\boldsymbol{\theta}} C$ by

$$F(\bar{t}; \boldsymbol{\theta}) := \int_0^{\bar{t}} \frac{1}{\sigma^2(s)} \nabla_{\boldsymbol{\theta}} f(s; \boldsymbol{\theta}) \nabla_{\boldsymbol{\theta}} f(s; \boldsymbol{\theta})^T dP(s)$$

where $F(\bar{t}; \boldsymbol{\theta})$ represents the so called generalized Fisher information matrix [12]. As a result of this analysis, Banks et al. analogously define the continuous generalized sensitivity functions as the diagonal elements of $F(\bar{t}; \boldsymbol{\theta})^{-1} f(t; \boldsymbol{\theta})$ or

$$gs(t; \boldsymbol{\theta}) = \int_0^t \left(F(\bar{t}; \boldsymbol{\theta})^{-1} \frac{1}{\sigma^2(s)} \nabla_{\boldsymbol{\theta}} f(s; \boldsymbol{\theta}_0) \right) \bullet \nabla_{\boldsymbol{\theta}} f(s; \boldsymbol{\theta}_0) dP(s), \quad t \in [0, \bar{t}]. \tag{4.19}$$

As a tool to prevent misleading conclusions from a potential FTOA, Banks et al. further introduce the time derivative of $gs(t; \theta)$

$$\frac{\partial}{\partial t} gs(t; \boldsymbol{\theta}) := \left(F(\bar{t}; \boldsymbol{\theta})^{-1} \frac{1}{\sigma^2(s)} \nabla_{\boldsymbol{\theta}} f(t; \boldsymbol{\theta}_0) \right) \bullet \nabla_{\boldsymbol{\theta}} f(t; \boldsymbol{\theta}_0). \tag{4.20}$$

In our subsequent work, we denote this quanity (4.20) as $gs_{RIA}(t;\boldsymbol{\theta}) = \frac{\partial}{\partial t}gs(t;\theta)$, i.e., the **rate of information acquisition** (RIA) at a specific point in $\mathcal{D}$.

4.1.3 Continuous PDE-Based GSFs (PGSFs)

In the OGSFs studies, the nonlinear regression function, $f(t;\boldsymbol{\theta})$, contains one independent variable, and a vector of parameters. For general size-structured population, continuous PDE models, we adapt the nonlinear regression function to depended on a column vector of independent variables, which we denote as $\mathbf{r} = [r_1, r_{2,} \dots, r_{N_r}]^T$ with dimension N_r. For example, in the analysis of the OGSFs in Sections 4.1.1 and 4.1.2, $N_r = 1$ and $r_1 = t$, whereas with the Smoluchowski coagulation PDE, $N_r = 2$ and $[r_1, r_2] = [t, x]$. Without loss of generality, we also let $r_i \in [0, \overline{r}_i]$ for each $i \in [1, 2, \dots, N_r]$, where $\overline{r}_i$ represents the maximum values of each independent variable respectively, and we denote the vector of maximum independent variable values $\overline{\mathbf{r}} = [\overline{r}_1, \overline{r}_2, \dots, \overline{r}_{N_r}]^T$. From the continuous OGSFs defined by Banks et al. in [11], we can then make the straight forward extension for the Fisher information matrix

$$F(\overline{\mathbf{r}};\boldsymbol{\theta}) := \int_0^{\overline{r}_{N_r}} \int_0^{\overline{r}_{N_r-1}} \cdots \int_0^{\overline{r}_1} \frac{1}{\sigma^2(\mathbf{r})} \nabla_{\boldsymbol{\theta}} f(\mathbf{r};\boldsymbol{\theta}) \nabla_{\boldsymbol{\theta}} f(\mathbf{r};\boldsymbol{\theta})^T dr_1 dr_2 \dots dr_{N_r} \,,$$

and to the continuous PGSFs,

$$gs(\mathbf{r};\boldsymbol{\theta}) = \int_0^{r_{N_r}} \int_0^{r_{N_r-1}} \cdots \int_0^{r_1} \frac{1}{\sigma^2(\mathbf{r})} \left(F(\overline{\mathbf{r}};\boldsymbol{\theta})^{-1} \frac{1}{\sigma^2(\mathbf{r})} \nabla_{\boldsymbol{\theta}} f(\mathbf{r};\boldsymbol{\theta}_0) \right) \bullet \nabla_{\boldsymbol{\theta}} f(\mathbf{r};\boldsymbol{\theta}_0) dr_1 dr_2 \dots dr_{N_r} \quad \boldsymbol{\theta} \in \mathbb{R}^L \,.$$

We also extend (4.20) to a **rate of information acquisition** (RIA) for the PGSFs

$$gs_{RIA}(\mathbf{r};\boldsymbol{\theta}) = \frac{\partial^{N_r}}{\partial r_{N_r} \partial r_{N_r-1} \cdots \partial r_1} gs(\mathbf{r};\boldsymbol{\theta}) := \left(F(\overline{\mathbf{r}};\boldsymbol{\theta})^{-1} \frac{1}{\sigma^2(\mathbf{r})} \nabla_{\boldsymbol{\theta}} f(\mathbf{r};\boldsymbol{\theta}_0) \right) \bullet \nabla_{\boldsymbol{\theta}} f(\mathbf{r};\boldsymbol{\theta}_0).$$

In this chapter, we examine size-structured populations in a general context, therefore we assume a constant variance of one and normal error distribution for all measurements. Furthermore, for our purposes, we adapt the nonlinear regression function so that f depends on two variables, t and x, and one parameter, γ, so that

$$gs(t, x; \gamma) = \frac{\int_0^t \int_0^x \left(\frac{\partial f}{\partial \gamma}\right)^2 dr ds}{\int_0^{\overline{t}} \int_0^{\overline{x}} \left(\frac{\partial f}{\partial \gamma}\right)^2 dr ds}, \tag{4.21}$$

where $\overline{t}$ and $\overline{x}$ represents the maximum values of time and volume respectively. Also, for the rate of information acquisition,

$$\begin{aligned} gs_{RIA}(t,x;\gamma) &:= \frac{\partial^2}{\partial t \partial x}\left[gs(t_k,x_s;\gamma)\right] && (4.22)\\ &= \frac{\partial^2}{\partial t \partial x}\left[\frac{\int_0^{t_k}\int_0^{x_s}\left(\frac{\partial f}{\partial \gamma}\right)^2 dxdt}{gs(\overline{t},\overline{x};\gamma)}\right] && (4.23)\\ &\approx \frac{\left(\frac{\partial f(t_k,x_s;\gamma)}{\partial \gamma}\right)^2}{gs(\overline{t},\overline{x};\gamma)}. && (4.24)\end{aligned}$$

4.1.4 Determining the optimum subdomain, $\mathcal{D}^*$

In [84], Thomaseth and Cobelli only offer a visual analysis of how we can apply the OGSFs to determine $\mathcal{D}^*$. In [11], Banks et al. propose a mathematical implementation to determine the upper bound of $\mathcal{D}^*$ by bounding the TSFs variation. In this section, we offer a quantitative means for computing the lower and upper bounds of an optimal $\mathcal{D}^*$. To determine the lower ends of $\mathcal{D}^*$, we consider a level curve that represents a fraction of the maximum RIA. Then to determine the upper ends of $\mathcal{D}^*$, we consider a second level curve that represents the points where the PGSFs approach a value of one.

First, we consider the RIA to determine the lower ends of $\mathcal{D}^*$. In the analysis that follows, we assume only two independent variables and one parameter with $\mathcal{D} = [\underline{t},\overline{t}] \times [\underline{x},\overline{x}]$.[4] We define the maximum gs_{RIA} as

$$\overline{gs}_{RIA} = \max_{(t,x)\in\mathcal{D}} \{|gs_{RIA}(t,x;\gamma)|\}.$$

Then we denote a fraction $\omega \in (0,1)$ of $\overline{gs}_{RIA}$and define the level curve, Γ_ω, where

$$\Gamma_\omega = \left\{(t,x) \mid |gs_{RIA}(t,x;\gamma)| = \omega \overline{gs}_{RIA}\right\},$$

and from that level curve, we find the minimum values of x and t, which we denote x_* and t_*, where $x_* = \min_x \Gamma_\omega$ and $t_* = \min_t \Gamma_\omega$.

Second, we consider the PGSFs to determine the upper ends of $\mathcal{D}^*$. We let ρ represent the proximity to one that we desire, and define the level curve, Γ^ρ, where

$$\Gamma^\rho = \left\{(t,x) \mid |1 - gs(t,x;\gamma)| = \rho\right\}.$$

---

[4] The inclusion of additional independent variables and parameters is straightforward.

Note that any point in the set Γ^ρ provides a satisfactory upper bound on $\mathcal{D}^*$. To determine a range of upper bounds depending on which independent variable costs more in terms of gathering data, we consider $x^* = \min_x \Gamma^\rho$ with its dependent $t(x^*)$, and $t^* = \min_t \Gamma^\rho$ with its dependent $x(t^*)$. We denote the optimum subdomain as $\mathcal{D}_x^*$, where

$$\mathcal{D}_x^* = [t_*, t(x^*)] \times [x_*, x^*],$$

when high resolution data in x is more expensive. Conversely, when high resolution data in t is more expensive, we denote the optimum subdomain as $\mathcal{D}_t^*$, where

$$\mathcal{D}_t^* = [t_*, t^*] \times [x_*, x(t^*)].$$

4.2 Application of PGSFs to the Smoluchowski coagulation equation

In practice, when we model experimental data, we often find that the measurements made by experimental devices can produce heteroscedasticity in the data, i.e., data with non-constant variation. An advantage of the OGSFs, in both the discrete and continuous versions, lies in their incorporation of a weighted residual sum of squares (WRSS), which allows for differing variance. In this context, the OGSFs give a greater weight to measurements with smaller variation.

Additionally, when we know specifically how the variance differs, we transform the model to overcome heteroscedasticity. For example, with many experimental devices, the measurement error grows with the size of the quantity measured resulting in a log-normal error distribution (as described in [21] and utilized in [20]). With log-normal error distribution, the analog of (4.1) would be

$$\log\left[y(t)\right] = \log\left[f(t, \boldsymbol{\theta})\right] + \epsilon\,.$$

With this change, the error, ϵ, has a normal distribution with zero mean and constant variance. However, for the purposes of this chapter, we only consider constant variance.

To illustrate an application of the PGSFs to the continuous model in (2.3), we choose three coagulation kernels, the constant, the additive, and the multiplicative, for which known solutions to (2.2) exist. In Section 4.2.1, we list the three solutions with proper placement of the constant parameter, γ. Additionally, we justify our choice of minimums for $\mathcal{D}$. Then in Section 4.2.2, we discuss the benefits and drawbacks of different choices for the order of summation when calculating the PGSFs.

4.2.1 Set up

Before we implement the PGSFs on the general Smoluchowski coagulation equation, we must place the aggregation kernel parameter appropriately. Analytical solutions presented in the literature commonly assume a constant, $\gamma = 1$, in the aggregation kernels. For our generalized sensitivity analysis, we need to include the general constant because it constitutes the parameter of interest with respect to which we have to take derivatives. When $\gamma = 1$,

$$\frac{\partial f(t,x)}{\partial t} = \frac{1}{2}\int_0^x f(t,y)f(t,x-y)dy - f(x)\int_0^\infty f(t,y)dy,$$

which has the solution given by Aldous [5] for $K = 1$,

$$f(t,x) = \left(\frac{2}{t}\right)^2 e^{\frac{-2x}{t}}.$$

Now consider the Smoluchowski coagulation equation with scaling γt,

$$\begin{aligned}\frac{\partial f(\gamma t,x)}{\partial\,(\gamma t)} &= \frac{\partial f(\gamma t,x)}{\gamma\partial t}\\ &= \frac{1}{2}\int_0^x K(y,x-y)f(\gamma t,y)f(\gamma t,x-y)dy - f(\gamma t,x)\int_0^\infty K(x,y)f(\gamma t,y)dy\end{aligned}$$

therefore

$$\frac{\partial f(\gamma t,x;\gamma)}{\partial t} = \frac{1}{2}\int_0^x \gamma f(\gamma t,y)f(\gamma t,x-y)dy - f(\gamma t,x)\int_0^\infty \gamma f(\gamma t,y)dy$$

where the adapted solution to [5] for $K = \gamma$ is

$$f(\gamma t,x) = \left(\frac{2}{\gamma t}\right)^2 e^{\frac{-2x}{\gamma t}}. \tag{4.25}$$

Similar analysis leads to the general solutions we use for all three kernels considered in our work on PGSFs. In Table 4.1, we list the three kernels studied in this work and the source of the known solution. Note that analytical solutions presented in the literature commonly assume a constant, $\gamma = 1$, in the aggregation kernels. We aim to identify the value of γ, so we incorporate it as the general constant.

$K(x,y)$	$f(t,x;\gamma)$ for general constant, $\gamma \in \mathbb{R}_+ < \infty$	Source
γ	$f(t,x;\gamma) = \left(\frac{2}{\gamma t}\right)^2 e^{\frac{-2x}{\gamma t}},\ x \in [0,\infty), \gamma t \in (0,\infty)$	Aldous [5]
$\gamma(x+y)$	$\frac{1}{\sqrt{2\pi}} x^{-3/2} \left(e^{-\gamma t}\right) e^{-x/\left(2e^{2\gamma t}\right)},\ x \in (0,\infty), \gamma t \in [0,\infty)$	Menon and Pego [66]
γxy	$\frac{1}{\sqrt{2\pi}} x^{-5/2} e^{-(1-\gamma t)^2 x/2},\ x \in (0,\infty), \gamma t \in [0,1)$	Menon and Pego [66]

Table 4.1: Solutions to the Smoluchowski coagulation equation

The PGSFs are defined on a domain which starts at a point $\mathbf{0} \in \mathbb{R}^N$. For our purposes, the PGSFs incorporate $\left(\frac{\partial f}{\partial \gamma}\right)^2$, so when we examine the lower ends of $\mathcal{D}$, we must consider the limit as $t, x \to 0^+$ of $\left(\frac{\partial f}{\partial \gamma}\right)^2$. As an example, consider the constant kernel where

$$\frac{\partial f}{\partial \gamma} = \frac{8}{t^2 \gamma^3} e^{\frac{-2x}{\gamma t}} \left[\frac{x}{t\gamma} - 1\right].$$

Choosing the path along $x = 0$ demonstrates an infinite limit,

$$\begin{aligned} \lim_{(t,0)\to(0^+,0^+)} \left(\frac{\partial f}{\partial \gamma}\right)^2 &= \lim_{(t,0)\to(0^+,0^+)} \frac{64}{t^4 \gamma^6} e^{\frac{-4x}{\gamma t}} \left[\frac{x}{t\gamma} - 1\right]^2 \\ &= \lim_{(t,0)\to(0^+,0^+)} \frac{64}{t^4 \gamma^6}. \end{aligned} \tag{4.26}$$

The infinite limit in (4.26) helps guide our choice of $\underline{t} = 0.2$ because it ensures our PGSFs calculations remain within computer precision. Similar analysis leads to choices of $\underline{x} = 0.1$ for both the additive kernel and the multiplicative kernel. In Appendix C, we present similar calculations in detail for all three kernels, justifying the choice of the lower bounds in each case.

4.2.2 Summation choices for calculating PGSFs

We note that in (4.21), one is faced with a choice of which variable is summed first. This choice is not encountered in the OGSFs context. To calculate the generalized sensitivity, we can calculate the numerator in (at least) three ways.

One possible choice, which we designate as the **Simultaneously Incremental** (SI) method, involves summing along the spatial axis to x_s with $s = 1, \ldots, N_x$ and then incrementing time as depicted in

Figure 4.1a. For the SI method,

$$\begin{aligned} gs_{SI}(t_k, x_s; \gamma) &= \frac{\int_0^{t_k}\int_0^{x_s}\left(\frac{\partial f}{\partial \gamma}\right)^2 dxdt}{gs(\bar{t}, \bar{x}; \gamma)} \\ &\approx \frac{\sum_{i=1}^{k}\sum_{j=1}^{s}\left(\frac{\partial f}{\partial \gamma}(t_i, x_j; \gamma)\right)^2 \Delta x_j \Delta t_i}{gs(\bar{t}, \bar{x}; \gamma)}, \end{aligned} \tag{4.27}$$

where $\Delta x_j = x_{j+1} - x_j$ and $\Delta t_j = t_{j+1} - t_j$, where N_x represents the number of volume points. Unless otherwise specified, we space our grids uniformly. Note that in (4.27), the order of summation does not matter.

We designate the second method, the **All Size, Incremental in Time** (ASIT) method, with which we sum along the entire size-axis before we increment time as depicted in Figure 4.1b. For the ASIT method, we denote $(t_k, x_s) = (t, x)_i$ such that $i = s + (k-1)N_x$ with $k = 1, 2, \ldots, N_t$ and $s = 1, 2, \ldots, N_x$. Then for the ASIT method,

$$\begin{aligned} gs_{ASIT}((t,x)_i; \gamma) = gs_{ASIT}(t_k, x_s; \gamma) &= \frac{\int_0^{t_k}\int_0^{x_s}\left(\frac{\partial f}{\partial \gamma}\right)^2 dxdt}{gs(\bar{t}, \bar{x}; \gamma)} \\ &\approx \frac{\sum_{j=1}^{i}\left(\frac{\partial f}{\partial \gamma}((t,x)_j; \gamma)\right)^2 \Delta x_j \Delta t_j}{gs(\bar{t}, \bar{x}; \gamma)}. \end{aligned}$$

Lastly, we designate the third method, the **All Time, Incremental in Size** (ATIS) method, with which we sum along the entire time-axis before we increment the size dimension as depicted in Figure 4.1b. In this case, we denote $(t_k, x_s) = (t, x)_i$ such that $i = k + (s-1)N_t$ with $k = 1, 2, \ldots, N_t$ and $s = 1, 2, \ldots, N_x$. Therefore

$$\begin{aligned} gs_{ATIS}((t,x)_j; \gamma) = gs_{ATIS}(t_k, x_s; \gamma) &= \frac{\int_0^{t_k}\int_0^{x_s}\left(\frac{\partial f}{\partial \gamma}\right)^2 dxdt}{gs(\bar{t}, \bar{x}; \gamma)} \\ &\approx \frac{\sum_{i=1}^{j}\left(\frac{\partial f}{\partial \gamma}((t,x)_i; \gamma)\right)^2 \Delta x_j \Delta t_j}{gs(\bar{t}, \bar{x}; \gamma)}. \end{aligned}$$

For all three methods, we compute the denominator of our generalized sensitivity,

$$\begin{aligned} gs(\bar{t}, \bar{x}; \gamma) &= \int_0^{\bar{t}}\int_0^{\bar{x}}\left(\frac{\partial f}{\partial \gamma}(t, x; \gamma)\right)^2 dxdt \\ &= \sum_{i=1}^{N_t-1}\int_{t_i}^{t_{i+1}}\sum_{j=1}^{N_x-1}\int_{x_j}^{x_{j+1}}\left(\frac{\partial f}{\partial \gamma}(t, x; \gamma)\right)^2 dxdt \qquad (4.28) \\ &\approx \sum_{i=1}^{N_t-1}\sum_{j=1}^{N_x-1}\left(\frac{\partial f}{\partial \gamma}(t_i, x_j; \gamma)\right)^2 \Delta x_j \Delta t_i. \qquad (4.29) \end{aligned}$$

Note that this scheme represents choosing the lower left corner of the subcolumns to approximate the integration. In Section 4.3, we offer justification for calculating the PGSFs via the SI method rather than via either the ASIT or ATIS methods.

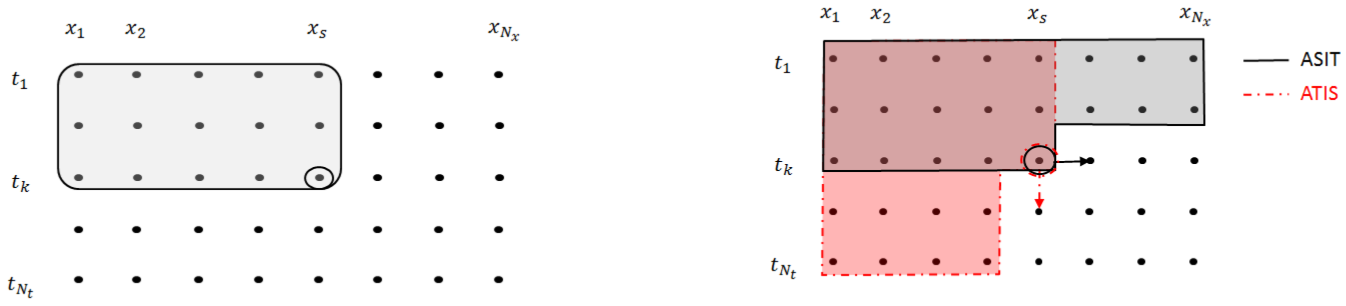

(a) SI Method

(b) ASIT and ATIS Methods

Figure 4.1: Summation methods - in (4.21), one is faced with a choice of which variable is summed first. In (a), which depicts the **Simultaneously Incremental** (SI) Method, the order of summation does not matter. The box encloses the set of points which indicates summing in x to x_s and then incrementing time or summing in t to t_k and then incrementing size. In (b), the solid line (the **All Size, Incremental in Time** (ASIT) Method) depicts summing along the entire size axis before we increment time. Conversely, the dashed line in (b) (the **All Time, Incremental in Size** (ATIS) method) depicts summing along the entire t-axis before we increment size.

4.3 Determining $\mathcal{D}^*$ for the Smoluchowski coagulation equation with PGSFs

In order to apply the PGSFs concept to the Smoluchowski coagulation equation, we make several decisions. First, we choose three aggregation kernels, constant, additive, and multiplicative, for which known solutions exist. Next we choose $\mathcal{D}$ and the number of points on our grid. These choices need to provide enough information and enough resolution to extract a meaningful $\mathcal{D}^*$. We provide the details of the impacts of these choices later in this section. Finally, in order to compute the PGSFs, we choose the advocate for one of the three summation orders described in Section 4.2.2.

In the use of GSFs, a natural question concerns choosing the overall domain $\mathcal{D}$. For all three kernels, to choose the lower bounds ($\underline{x}$ and $\underline{t}$) of $\mathcal{D}$, we face the following dilemma concerning the FTOA.[5] After we determine $\underline{x}$ and $\underline{t}$, determining $\overline{x}$ and $\overline{t}$ in conjunction with grid spacing also presents difficulties. If

---

[5] Recall the FTOA is described in Section 4.2.1. We also expand upon this issue in Appendix C

we space the grid too widely, the PGSFs reach one on the first step, which does not provide a meaningful resolution. Furthermore, if we use maximum values for $\mathcal{D}$ that are too small, we face a potential FTOA as described in Section 4.1. To avoid this artifact, we examine the PGSFs curves and the RIA curves to ensure that the PGSFs curves stabilize at one well before the maximum domain limits and to confirm that the RIA stabilizes near zero. If we do not achieve both of those criteria, we need to increase $\overline{x}$ or $\overline{t}$ until we do. For all three kernels that we study, the PGSFs curves in Figures 4.3a , 4.4a, and 4.5a, do stabilize at one before $\overline{x}$ and $\overline{t}$, and the RIA stabilizes near zero in Figures 4.3b, 4.4b, and 4.5b.

The primary purpose of applying PGSFs in our study is to determine the subdomains, $\mathcal{D}^*$, that contain the most important information relative to estimating the constant, γ. In our application of the PGSFs to the Smoluchowski coagulation equation, we incorporate one parameter, therefore $\left(\frac{\partial f}{\partial \gamma}\right)^2$ provides the primary quantity of interest. As depicted in Figure 4.2a, for the constant kernel, we notice a large spike at small times and volumes. Then zooming in as depicted in Figure 4.2b, we notice more detail at volumes greater than approximately 0.2. The plots in Figure 4.2, do not clearly indicate the importance of the subdomain, $x \in [0.2, 0.6]$.

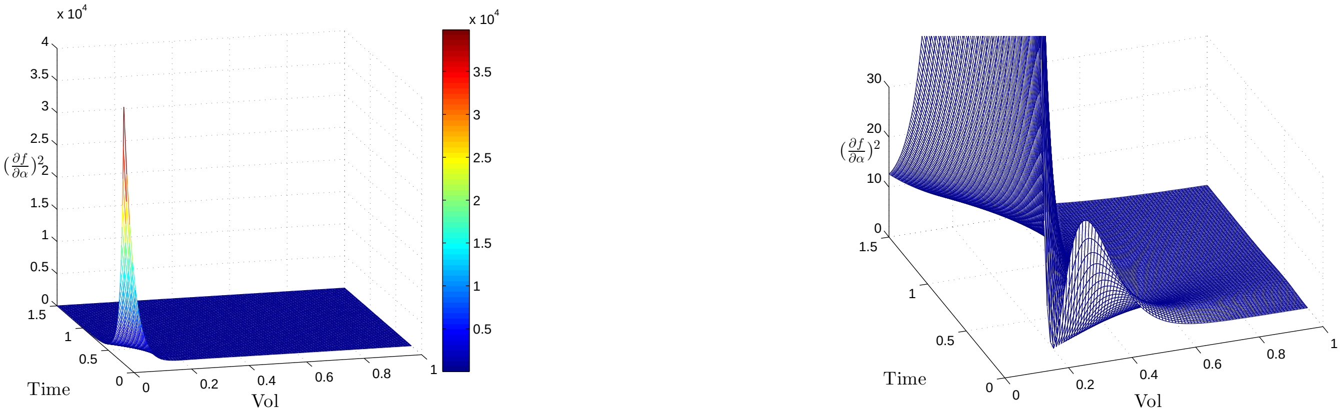

(a) Entire range

(b) Zoomed in

Figure 4.2: $\left(\frac{\partial f(t,x)}{\partial \gamma}\right)^2$vs. x and t for $K(x,y) = \gamma$: In (a) we plot the entire range which illustrates the spike at small time and small volume points, and in (b) we illustrate more detail away from the spike.

Conversely, the PGSFs and RIA plots allows us to quantify the relative importance of all the contributions. Figure 4.3 reveals the PGSFs approach one and the rates of information acquisition approach zero well within $\mathcal{D}$. By implementing the mathematical strategy in Section 4.1.4, we compute the lower bounds, $(t_*, x_*) = (0.2, 0)$, from Γ_ω and the upper bounds, which range from $(t(x^*), x^*) \approx (0.94, 0.11)$ to $(t^*, x(t^*)) \approx (0.56, 0.48)$, from Γ^ρ. We achieve these results (and the results for the other two kernels) by setting $\Delta t = \Delta x = .01$, $\omega = 0.5$, and $\rho = 0.1$ and by implementing the SI method described in Section 4.2.2.

(a) Contour plot of PGSFs vs. time and volume which we calculate via the SI method

(b) Contour plot of RIA vs. time and volume

Figure 4.3: Generalized Sensitivity and RIA for the constant kernel - subregions where the largest rates of change occur as the PGSFs transition from zero to one indicate an approximate $\mathcal{D}^*$. The rectangles in (a) represent optimum subdomains, $\mathcal{D}^*_x$ and $\mathcal{D}^*_t$, as summarized in Table 4.2.

We can determine $\mathcal{D}^*$ for the additive and multiplicative kernels by performing similar assessments of the PGSFs plots (in Figures 4.4a and 4.5a) to ensure we avoid the FTOA. We then confirm that the rates approach zero in those subdomains in Figures 4.4b and 4.5b respectively. By implementing the mathematical strategy in Section 4.1.4 for the additive kernel, we compute the lower bounds, $(t_*, x_*) = (0.42, 0.1)$, and the upper bounds, which range from $(t(x^*), x^*) \approx (4.27, 0.28)$ to $(t^*, x(t^*)) \approx (2.69, 0.94)$. For the multiplicative kernel, we compute the lower bounds, $(t_*, x_*) = (0.24, 0.1)$, and the upper bounds, which range from $(t(x^*), x^*) \approx (0.920.28)$ to $(t^*, x(t^*)) \approx (0.76, 0.75)$. We summarize $\mathcal{D}^*$ for each aggregation kernel in Table 4.2.

$K(x,y)$	$\mathcal{D}_x^* = [t_*, t(x^*)] \times [x_*, x^*]$	$\mathcal{D}_t^* = [t_*, t^*] \times [x_*, x(t^*)]$	Gelation Time
γ	$[0.2, 0.94] \times [0, 0.11]$	$[0.2, 0.56] \times [0, 0.48]$	
$\gamma(x+y)$	$[0.42, 4.27] \times [0.1, 0.28]$	$[0.42, 2.69] \times [0.1, 0.94]$	
γxy	$[0.24, 0.92] \times [0.1, 0.28]$	$[0.24, 0.76] \times [0.1, 0.75]$	$t = \frac{1}{\gamma}$

Table 4.2: Summary of $\mathcal{D}^*$ when estimating the constant in three aggregation kernels for the Smoluchowski coagulation equation. We achieve these results by setting $\Delta t = \Delta x = .01$, $\omega = 0.5$, and $\rho = 0.1$ and by implementing the SI method described in Section 4.2.2. The second column reflects an optimum subdomain when volume data is more costly and the third column denotes an optimum subdomain when the time data is more costly. Note that the time subdomain for the multiplicative kernel indicates that the pertinent information occurs prior to gelation.

The PGSFs for the multiplicative kernel provide another important result. It is well known that **gelation** occurs for the multiplicative kernel[6] . When gelation occurs the system experiences growth rapid enough that aggregates with **infinite** volume develop in finite time [89]. Mass is not physically lost, but the aggregates with **infinite** volume possess fundamentally different mathematical properties than the individual aggregates that make up the gel. We direct the interested reader to [93], in which Ziff and Stell provide a thorough description of the implications of various assumptions on the post-gelation behavior of the solutions and of the moments. As summarized in Table 4.2, our results provide evidence that the pertinent information necessary for estimating the constant in $K(x,y) = \gamma xy$ occurs well before gelation.

---

[6] With the multiplicative kernel, gelation occurs at $t = \frac{1}{\gamma}$.

(a) Contour plot of PGSFs vs. time and volume which we calculate via the SI method

(b) Contour plot of RIA vs. time and volume

Figure 4.4: Generalized Sensitivity and RIA for the additive kernel - subregions where the largest rates of change occur as the PGSFs transition from zero to one indicate an approximate $\mathcal{D}^*$. The rectangles in (a) represent optimum subdomains, $\mathcal{D}_x^*$ and $\mathcal{D}_t^*$, as summarized in Table 4.2.

(a) Contour plot of PGSFs vs. time and volume which we calculate via the SI method

(b) Contour plot of RIA vs. time and volume

Figure 4.5: Generalized Sensitivity and RIA for the multiplicative kernel - subregions where the largest rates of change occur as the PGSFs transition from zero to one indicate an approximate $\mathcal{D}^*$. The rectangles in (a) represent optimum subdomains, $\mathcal{D}_x^*$ and $\mathcal{D}_t^*$, as summarized in Table 4.2.

Finally, as described in Section 4.2.2, we examined three summation methods when calculating the PGSFs. We plot the constant kernel PGSFs for each of the three methods in Figure 4.6. The ASIT method indicates the approximate $\bar{t}$ necessary for the generalized sensitivity to reach one, but it does not provide an obvious indication of $\bar{x}$. Conversely, the ATIS method indicates the necessary $\bar{x}$ for the generalized sensitivity to reach one, but it does not provide useful information relative to the time domain. However, the SI method simultaneously illustrates a combination of the ASIT and ATIS methods and provides both time and volume indications of where the generalized sensitivity reaches one. We achieve similar results for the additive and multiplicative kernels. Note that regardless of the summation scheme we use, the RIA remains the same.

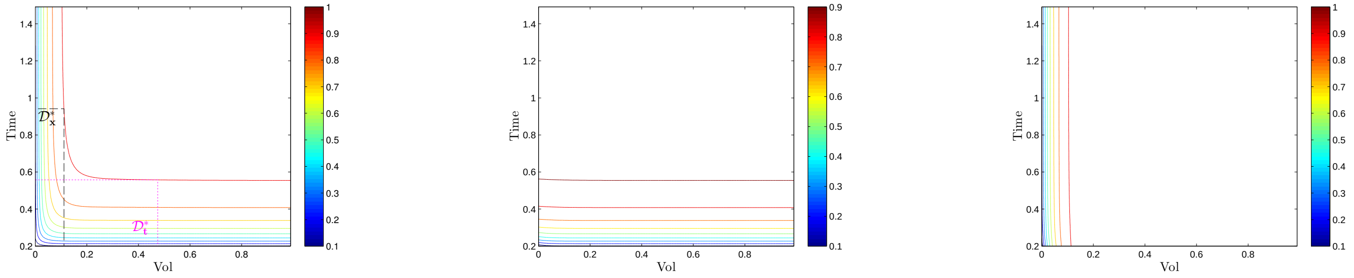

(a) SI Method

(b) ASIT Method

(c) ATIS Method

Figure 4.6: Comparison of the the three summation methods for calculating the PGSFs for the constant kernel: in (a), we sum along x to x_s and then increment time. In (b), we sum along x to x_{N_x} and then increment time. In (c), we sum along t to t_{N_t} and then increment volume. Note that the SI method illustrates a combination of the ASIT and ATIS methods providing both time and volume indications of where the generalized sensitivity reaches one on the same plot.

4.4 Conclusions and Future Work

In this chapter, we have extended the concepts of the ODE-based GSFs introduced by Thomaseth and Cobelli in [84], to the PDE-based GSFs. These PGSFs provide a framework for determining an optimum subdomain, $\mathcal{D}^*$, for size-structured population, PDE models. We then apply PGSFs to the Smoluchowski coagulation equation, a popular size-structured population model, to determine $\mathcal{D}^*$ for parameter estimation in the constant, additive, and multiplicative kernels.

To accomplish the goal of determining optimal experimental domains, we offer a novel mathematical means of determining the entire $\mathcal{D}^*$ from generalized sensitivity functions. Specifically for the Smoluchowski coagulation equation, we determine that pertinent information for estimating the constant parameter, γ, occurs in small volume subdomains. When time data costs less than volume data, we generally require no larger than $x \approx 0.3$. We require no larger than $x \approx 0.94$ when time data is more costly than volume data.

We also determine that the most relevant time information occurs early in a coagulation experiment. How early varies widely among the three kernels with maximum times ranging from 0.56 to 4.27. Our study also acknowledges the potential for a **forced to one artifact**, FTOA, which is a known weakness of the generalized sensitivity functions. By addressing this weakness, we determine maxima in $\mathcal{D}$ which eliminate the artifact. Finally, we also provide results which indicate that all of the relevant time information for the multiplicative kernel occurs prior to gelation.

With our application to the Smoluchowski coagulation equation, we include only one parameter to estimate. Generally, PGSFs allows accounting for multiple parameters, and in our future work we aspire to study more sophisticated aggregation kernels which contain multiple parameters. As is popular in much of the literature, we will examine kernels of the form, $K(x, y) = \gamma(x^{\mu}y^{\nu} + x^{\nu}y^{\mu})$.

Lastly, in this work, we study the Smoluchowski coagulation equation, which models processes involving aggregation only. In the future, we would like to consider the Smoluchowski coagulation-fragmentation equation for which we would estimate both aggregation and fragmentation parameters.

Bibliography

[1] A. S. Ackleh. Parameter estimation in a structured algal coagulation-fragmentation model. **Nonlinear Analysis**, 28(5):837–854, Mar. 1997.

[2] A. S. Ackleh and B. G. Fitzpatrick. Modeling aggregation and growth processes in an algal population model: analysis and computations. **J. Math. Biology**, 35(4):480–502, Mar. 1997.

[3] A. S. Ackleh, B. G. Fitzpatrick, and T. G. Hallam. Approximation and parameter estimation problems for algal aggregation models. **Math. Models Methods Appl. Sci**, 4(3):291–311, 1994.

[4] A. S. Ackleh, T. G. Hallam, and H. C. Muller-Landau. Estimation of sticking and contact efficiencies in aggregation of phytoplankton: The 1993 SIGMA tank experiment. **Deep Sea Research Part II: Topical Studies in Oceanography**, 42(1):185–201, Jan. 1995.

[5] D. J. Aldous. Deterministic and Stochastic Models for Coalescence (Aggregation, Coagulation): A Review of the Mean-Field Theory for Probabilists. **Bernoulli**, 5(1):3–48, 1999.

[6] T. A. Bak and O. Heilmann. A finite version of Smoluchowski's coagulation equation. **Journal of Physics A: Mathematical and General**, 24(20):4889–4893, Oct. 1991.

[7] J. M. Ball and J. Carr. The discrete coagulation-fragmentation equations: Existence, uniqueness and density conservation. **J. Statistical Physics**, pages 203–234, 1990.

[8] J. M. Ball, J. Carr, and O. Penrose. The Becker-Doring cluster equations: Basic properties and asymptotic behaviour of solutions. **Communications in Mathematical Physics**, 104(4):657–692, Dec. 1986.

[9] H. T. Banks, M. Davidian, J. R. Samuels, and K. L. Sutton. Chapter 11: Mathematical and Statistical Estimation Approaches in Epidemiology. In G. Chowell, J. M. Hyman, L. M. A. Bettencourt, and C. Castillo-Chavez, editors, **Mathematical and Statistical Estimation Approaches in Epidemiology**, pages 249–302. Springer Netherlands, Dordrecht, 2009.

[10] H. T. Banks, S. Dediu, S. L. Ernstberger, and F. Kappel. Sensitivity functions and their uses in inverse problems. **Journal of Inverse and Ill-posed Problems jiip**, 15(7):683–708, 2008.

[11] H. T. Banks, S. Dediu, S. L. Ernstberger, and F. Kappel. Generalized sensitivities and optimal experimental design. **Journal of Inverse and Ill-posed Problems**, 18(1):25–83, Apr. 2010.

[12] H. T. Banks, K. Holm, and F. Kappel. Comparison of Optimal Design Methods in Inverse Problems. **Inverse problems**, 27(7):075002, July 2011.

[13] H. T. Banks and F. Kappel. Transformation semigroups andL 1-approximation for size structured population models. **Semigroup Forum**, 38(1):141–155, Dec. 1989.

[14] H. T. Banks and K. Kunisch. **Estimation Techniques for Distributed Parameter Systems**, volume 1 of **Systems \& Control: Foundations \& Applications**. Birkhäuser, Boston, MA, 1989.

[15] J. C. Barrett and J. S. Jheeta. Improving the accuracy of the moments method for solving the aerosol general dynamic equation. **Journal of Aerosol Science**, 27(8):1135–1142, Dec. 1996.

[16] J. Batzel, G. Baselli, R. Mukkamala, and K. H. Chon. Modelling and disentangling physiological mechanisms: linear and nonlinear identification techniques for analysis of cardiovascular regulation. **Philosophical transactions. Series A, Mathematical, physical, and engineering sciences**, 367(1892):1377–91, Apr. 2009.

[17] J. J. Batzel, F. Kappel, D. Schneditz, and H. T. Tran. **Cardiovascular and Respiratory Systems: Modeling, Analysis, and Control**, volume 14. SIAM, 2007.

[18] B. J. Berne and R. Pecora. **Dynamic Light Scattering: With Applications to Chemistry, Biology, and Physics**. Courier Dover Publications, 2000.

[19] R. Bordás, V. John, E. Schmeyer, and D. Thévenin. Numerical methods for the simulation of a coalescence-driven droplet size distribution. **Theoretical and Computational Fluid Dynamics**, 27(3-4):253–271, July 2012.

[20] D. M. Bortz, T. L. Jackson, K. A. Taylor, A. P. Thompson, and J. G. Younger. {\it Klebsiella pneumoniae} flocculation dynamics. **Bull. Math. Biology**, 70(3):745–68, Apr. 2008.

[21] R. J. Carroll and D. Ruppert. **Transformation and Weighting in Regression**. Chapman and Hall, 1988.

[22] A. Corradin, B. Di Camillo, V. Ciminale, G. Toffolo, and C. Cobelli. Sensitivity analysis of retrovirus HTLV-1 transactivation. **Journal of computational biology : a journal of computational molecular cell biology**, 18(2):183–93, Feb. 2011.

[23] J. M. Cushing. **An Introduction to Structured Population Dynamics**. SIAM, Philadelphia, PA, 1987.

[24] J. M. Cushing. Some competition models for size-structured populations. **Rocky Mountain Journal of Mathematics**, 20(4):879–897, Dec. 1990.

[25] F. P. da Costa. Existence and Uniqueness of Density Conserving Solutions to the Coagulation-Fragmentation Equations with Strong Fragmentation. **Journal of Mathematical Analysis and Applications**, 192(3):892–914, June 1995.

[26] F. P. da Costa. A Finite-Dimensional Dynamical Model for Gelation in Coagulation Processes. **Journal of Nonlinear Science**, 8(6):619–653, Dec. 1998.

[27] J. David, H. Tran, and H. T. Banks. HIV model analysis and estimation implementation under optimal control base treatment strategies. **International Journal of Pure and Applied Mathematics**, 57(No. 3):357–392, 2009.

[28] M. Doumic. Analysis of a Population Model Structured by the Cells Molecular Content. **Mathematical Modelling of Natural Phenomena**, 2(3):121–152, June 2008.

[29] M. Doumic, M. Hoffmann, P. Reynaud-Bouret, and V. Rivoirard. Nonparametric Estimation of the Division Rate of a Size-Structured Population. **SIAM Journal on Numerical Analysis**, 50(2):925–950, Jan. 2012.

[30] M. Doumic, P. Maia, and J. P. Zubelli. On the calibration of a size-structured population model from experimental data. **Acta biotheoretica**, 58(4):405–13, Dec. 2010.

[31] M. Doumic, B. Perthame, and J. P. Zubelli. Numerical solution of an inverse problem in size-structured population dynamics. **Inverse Problems**, 25(4):045008, Apr. 2009.

[32] M. Doumic and L. M. Tine. Estimating the division rate for the growth-fragmentation equation. **Journal of mathematical biology**, 67(1):69–103, July 2013.

[33] M. Doumic Jauffret and P. Gabriel. Eigenelements of a general aggregation-fragmentation model. **Mathematical Models and Methods in Applied Sciences**, 20(05):757–783, May 2010.

[34] R. L. Drake. A General Mathematical Survey of the Coagulation Equation. In G. M. Hidy and J. R. Brock, editors, **Topics in Current Aerosol Research (Part 2)**, volume 3 of **International Reviews in Aerosol Physics and Chemistry**, pages 201–376. Pergamon Press, New York, NY, 1972.

[35] P. B. Dubovskii. **Mathematical Theory of Coagulation**. Number 23 in Lecture Notes Series. Seoul National University, Research Institute of Mathematics, Global Analysis Research Center, Seoul National University, Seoul 151-742, Korea, 1994.

[36] P. B. Dubovskii and I. W. Stewart. Existence, Uniqueness and Mass Conservation for the Coagulation-Fragmentation Equation. **Mathematical Methods in the Applied Sciences**, 19(7):571–591, May 1996.

[37] M. R. Easterling, S. P. Ellner, and P. M. Dixon. Size-specific sensitivity: applying a new structured population model. **Ecology**, 81(3):694–708, Mar. 2000.

[38] B. Ebenman and L. Persson, editors. **Size-Structured Populations**. Springer Berlin Heidelberg, Berlin, Heidelberg, 1988.

[39] M. H. Ernst, R. M. Ziff, and E. M. Hendriks. Coagulation processes with a phase transition. **Journal of Colloid and Interface Science**, 97(1):266–277, Jan. 1984.

[40] M. Escobedo, P. Laurençot, S. Mischler, and B. Perthame. Gelation and mass conservation in coagulation-fragmentation models. **Journal of Differential Equations**, 195(1):143–174, Nov. 2003.

[41] M. Escobedo, S. Mischler, and B. Perthame. Gelation in Coagulation and Fragmentation Models. **Communications in Mathematical Physics**, 231(1):157–188, Aug. 2002.

[42] M. Escobedo, S. Mischler, and M. Rodriguez Ricard. On self-similarity and stationary problem for fragmentation and coagulation models. **Annales de l'Institut Henri Poincare (C) Non Linear Analysis**, 22(1):99–125, Jan. 2005.

[43] F. Filbet and P. Laurençot. Numerical Simulation of the Smoluchowski Coagulation Equation. **SIAM Journal on Scientific Computing**, 25(6):2004, 2004.

[44] M. Fink, J. Batzel, and F. Kappel. Modeling the Human Cardiovascular Control Response to Blood Volume Loss Due to Hemorrhage. **Biomedical Engineering**, L:145–152, 2006.

[45] M. Fink, J. J. Batzel, and H. Tran. A respiratory system model: parameter estimation and sensitivity analysis. **Cardiovascular engineering (Dordrecht, Netherlands)**, 8(2):120–34, June 2008.

[46] N. Fournier and P. Laurençot. Well-posedness of Smoluchowski's coagulation equation for a class of homogeneous kernels. **Journal of Functional Analysis**, 233(2):351–379, Apr. 2006.

[47] R. D. Guy, A. L. Fogelson, and J. P. Keener. Fibrin gel formation in a shear flow. **Mathematical Medicine and Biology**, 24(1):111–130, 2007.

[48] T. Ki{\o}rboe. Formation and fate of marine snow: small-scale processes with large-scale implications. **Scientia marina**, 65:57–71, 2001.

[49] F. E. Kruis, A. Maisels, and H. Fissan. Direct simulation Monte Carlo method for particle coagulation and aggregation. **AIChE Journal**, 46(9):1735–1742, Sept. 2000.

[50] A. Kumar, P. Laurençot, and G. Warnecke. Nonlinear Analysis Weak solutions to the continuous coagulation equation with multiple fragmentation. **Nonlinear Analysis**, 75(4):2199–2208, 2012.

[51] J. Kumar, G. Warnecke, M. Peglow, and S. Heinrich. Comparison of numerical methods for solving population balance equations incorporating aggregation and breakage. **Powder Technology**, 189(2):218–229, Jan. 2009.

[52] P. Laurençot. On a Class of Continuous Coagulation-Fragmentation Equations. **Journal of Differential Equations**, 167(2):245–274, Nov. 2000.

[53] P. Laurençot. Self-similar solutions to a coagulation equation with multiplicative kernel. **Physica D: Nonlinear Phenomena**, 222(1-2):80–87, Oct. 2006.

[54] P. Laurençot and S. Mischler. From the discrete to the continuous coagulation-fragmentation equations. **Proceedings of the Royal Society of Edinburgh: Section A Mathematics**, 132(05):1219, July 2002.

[55] P. Laurençot and S. Mischler. Convergence to equilibrium for the continuous coagulation-fragmentation equation. **Bulletin des Sciences Mathématiques**, 127(3):179–190, May 2003.

[56] M. H. Lee. On the Validity of the Coagulation Equation and the Nature of Runaway Growth. **Icarus**, 143(1):74–86, Jan. 2000.

[57] M. H. Lee. A survey of numerical solutions to the coagulation equation. **Journal of Physics A: Mathematical and General**, 34(47):10219–10241, Nov. 2001.

[58] E. Lehmann and G. Casella. **Theory of Point Estimation (Google eBook)**. Springer, 2nd edition, 1998.

[59] R. J. LeVeque. **Finite Difference Methods for Ordinary and Partial Differential Equations: Steady-State and Time-Dependent Problems**. SIAM, Philadelphia, PA, 2007.

[60] Y. Lin, K. Lee, and T. Matsoukas. Solution of the population balance equation using constant-number Monte Carlo. **Chemical Engineering Science**, 57:2241–2252, 2002.

[61] X. Lu. Conservation of Energy, Entropy Identity, and Local Stability for the Spatially Homogeneous Boltzmann Equation. **Journal of Statistical Physics**, 96(3-4):765–796, Aug. 1999.

[62] G. Madras and B. J. McCoy. Reversible crystal growth dissolution and aggregation breakage: numerical and moment solutions for population balance equations. **Powder Technology**, 143-144:297–307, June 2004.

[63] J. Maerz, R. Verney, K. Wirtz, and U. Feudel. Modeling flocculation processes: Intercomparison of a size class-based model and a distribution-based model. **Continental Shelf Research**, 31(10):S84–S93, July 2011.

[64] A. W. Mahoney and D. Ramkrishna. Efficient solution of population balance equations with discontinuities by finite elements. **Chemical Engineering Science**, 57:1107–1119, 2002.

[65] J. Makino, T. Fukushige, Y. Funato, and E. Kokubo. On the mass distribution of planetesimals in the early runaway stage. **New Astronomy**, 3(7):411–417, Nov. 1998.

[66] G. Menon and R. L. Pego. Dynamical Scaling in Smoluchowski's Coagulation Equations: Uniform Convergence. **SIAM Review**, 48(4):745, 2006.

[67] P. Michel. Existence of a solution to the cell division eigenproblem. **Mathematical Models and Methods in Applied Sciences**, 16(Julysupp01):1125–1153, 2006.

[68] P. Michel, S. Mischler, and B. Perthame. General entropy equations for structured population models and scattering. **Comptes Rendus Mathematique**, 338(9):697–702, May 2004.

[69] Z. Mimouni and J. Wattis. Similarity solution of coagulation equation with an inverse kernel. **Physica A: Statistical Mechanics and its Applications**, 388(7):1067–1073, Apr. 2009.

[70] H. Müller. Zur allgemeinen Theorie der raschen Koagulation. **Kolloidchemische Beihefte**, 27:257–311, 1928.

[71] R. Muraldir and D. Ramkrishna. An inverse problem in agglomeration kinetics. **J. Colloid \& Interface Science**, 112:348–361, 1986.

[72] H.-S. Niwa. School size statistics of fish. **Journal of theoretical biology**, 195(3):351–61, Dec. 1998.

[73] J. R. Norris. Uniqueness, nonuniqueness and a hydrodynamic limit for the stochastic coalescent. **Ann. Applied Probability**, 9:78–109, 1999.

[74] B. Perthame and L. Ryzhik. Exponential decay for the fragmentation or cell-division equation. **Journal of Differential Equations**, 210(1):155–177, Mar. 2005.

[75] B. Perthame and J. P. Zubelli. On the inverse problem for a size-structured population model. **Inverse Problems**, 23(3):1037–1052, June 2007.

[76] H. R. Pruppacher and J. D. Klett. **Microphysics of Clouds and Precipitation**. Riedel, Boston, MA, 1980.

[77] D. Ramkrishna. **Population Balances: Theory and Applications to Particulate Systems in Engineering**. Academic Press, San Diego, CA, 2000.

[78] M. Ranjbar, H. Adibi, and M. Lakestani. Numerical solution of homogeneous Smoluchowski's coagulation equation. **International Journal of Computer Mathematics**, 87(9):2113–2122, July 2010.

[79] U. Riebesell and D. A. Wolf-Gladrow. The relationship between physical aggregation of phytoplankton and particle flux: A numerical model. **Deep-Sea Research**, 39(7/8):1085–1102, 1992.

[80] H. M. Shapiro. **Practical Flow Cytometry**. John Wiley and Sons, 2005.

[81] J. Silk and S. D. White. The development of structure in the expanding universe. **The Astrophysical Journal**, 1978.

[82] L. G. Stanley and D. L. Stewart. **Design Sensitivity Analysis: Computational Issues of Sensitivity Equation Methods**. SIAM, 2002.

[83] M. P. Surh, J. B. Sturgeon, and W. G. Wolfer. Void nucleation, growth, and coalescence in irradiated metals. **Journal of Nuclear Materials**, 378(1):86–97, Aug. 2008.

[84] K. Thomaseth and C. Cobelli. Generalized Sensitivity Functions in Physiological System Identification. **Annals of Biomedical Engineering**, 27:607–616, 1999.

[85] S. Tuljapurkar and H. Caswell, editors. **Structured-Population Models in Marine, Terrestrial, and Freshwater Systems**. Population and Community Biology. Springer, 1997.

[86] M. van Smoluchowski. Drei Vortr{ä}ge {ü}ber Diffusion, Brownsche Bewegung und Koagulation von Kolloidteilchen. **Zeitschrift f{ü}r Physik**, 17:557–571, 1916.

[87] M. van Smoluchowski. Versuch einer mathematischen theorie der koagulation kinetic kolloider losungen. **Zeitschrift f{ü}r physikalische Chemie**, 92:129–168, 1917.

[88] D. Verkoeijen, G. A. Pouw, G. M. H. Meesters, and B. Scarlett. Population balances for particulate processes a volume approach. **Chemical Engineering Science**, 57(12):2287–2303, June 2002.

[89] J. A. D. Wattis. An introduction to mathematical models of coagulation-fragmentation processes: A discrete deterministic mean-field approach. **Physica D: Nonlinear Phenomena**, 222(1-2):1–20, Oct. 2006.

[90] B. Wennberg. An Example of Nonuniqueness for Solutions to the Homogeneous Boltzmann Equation. **Journal of Statistical Physics**, 95(1-2):469–477, Apr. 1999.

[91] Y. Yang and C.-W. Shu. Analysis of optimal superconvergence of discontinuous Galerkin method for linear hyperbolic equations. **SIAM Journal on Numerical Analysis**, 50(6):3110–3133, Jan. 2012.

[92] J. Zhe, A. Jagtiani, P. Dutta, J. Hu, and J. Carletta. A micromachined high throughput Coulter counter for bioparticle detection and counting. **Journal of Micromechanics and Microengineering**, 17(2):304–313, Feb. 2007.

[93] R. M. Ziff and G. Stell. Kinetics of polymer gelation. **The Journal of Chemical Physics**, 73(7):3492, 1980.

Appendix A

Example Calculation of Flux Derivative for FLFM

To illustrate how we calculate the right hand side of our second order spatial approximation in (2.20), we offer the following example set of calculations. At a given time step, k, consider $J_3^{N_x}(t_k)$. We have fixed $r = 3$, and then we fix $x_{mid(1)}$, therefore on a uniform grid, $\tilde{x} \geq x_3 - x_{mid(1)} = x_{mid(2)}$. We now know that $x_{mid(1)} + x_{mid(j)} \geq x_3$ for $j \in [2, N_x]$, so the contribution to $J_3^{N_x}(t_k)$ by aggregates in the first element is

$$\Delta x g_1^{N_x}(t_k)\left[\int_{x_{mid(2)}}^{x_3} \frac{K(x_{mid(1)}, y)}{y} g_2^{N_x}(t_k)dy + \sum_{j=3}^{N_x-1}\left(\int_{x_j}^{x_{j+1}} \frac{K(x_{mid(1)}, y)}{y} g_j^{N_x}(t_k)dy\right)\right].$$

We then consider contributions of aggregates with volume $x_{mid(2)}$, which leads to $\tilde{x} \geq x_3 - x_{mid(2)} = x_{mid(1)}$. This implies $j \in [1, N_x]$ for contributions to $J_3^{N_x}(t_k)$ by aggregates in the second element amounting to

$$\Delta x g_2^{N_x}(t_k)\left[\int_{x_{mid(1)}}^{x_2} \frac{K(x_{mid(1)}, y)}{y} g_1^{N_x}(t_k)dy + \sum_{j=2}^{N_x-1}\left(\int_{x_j}^{x_{j+1}} \frac{K(x_{mid(1)}, y)}{y} g_j^{N_x}(t_k)dy\right)\right].$$

We now have our total flux across x_3

$$\begin{aligned} J_3^{N_x}(t_k) &= \Delta x g_1^{N_x}(t_k)\left[\int_{x_{mid(2)}}^{x_3} \frac{K(x_{mid(1)}, y)}{y} g_2^{N_x}(t_k)dy + \sum_{j=3}^{N_x-1}\left(\int_{x_j}^{x_{j+1}} \frac{K(x_{mid(1)}, y)}{y} g_j^{N_x}(t_k)dy\right)\right] \\ &+ \Delta x g_2^{N_x}(t_k)\left[\int_{x_{mid(1)}}^{x_2} \frac{K(x_{mid(1)}, y)}{y} g_1^{N_x}(t_k)dy + \sum_{j=2}^{N_x-1}\left(\int_{x_j}^{x_{j+1}} \frac{K(x_{mid(1)}, y)}{y} g_j^{N_x}(t_k)dy\right)\right]. \end{aligned}$$

At this point, we can generalize the flux at any given element boundary $(i \in [2, N_x])$ as

$$J_i^{N_x}(t_k) = \sum_{p=1}^{i-1} \Delta x g_p^{N_x}(t_k)\left\{\int_{x_{mid(i-p)}}^{x_{i-p+1}} \frac{K(x_{mid(p)}, y)}{y} dy\, g_{i-p}^{N_x}(t_k) + \sum_{j=i-p+1}^{N_x-1} \int_{x_j}^{x_{j+1}} \frac{K(x_{mid(p)}, y)}{y} dy\, g_j^{N_x}(t_k)\right\}. \tag{A.1}$$

Specifically, when $K(x, y) \equiv 1$,

$$J_i^{N_x}(t_k) = \sum_{p=1}^{i-1} \Delta x g_p^{N_x}(t_k)\left\{\int_{x_{mid(i-p)}}^{x_{i-p+1}} \frac{1}{y} dy\, g_{i-p}^{N_x}(t_k) + \sum_{j=i-p+1}^{N_x-1} \int_{x_j}^{x_{j+1}} \frac{1}{y} dy\, g_j^{N_x}(t_k)\right\},$$

which after integration gives us

$$J_i^{N_x}(t_k) = \sum_{p=1}^{i-1} \Delta x g_p^{N_x}(t_k)\left\{\ln \frac{x_{i-p+1}}{x_{mid(i-p)}}\, g_{i-p}^{N_x}(t_k) + \sum_{j=i-p+1}^{N_x-1} \ln \frac{x_{j+1}}{x_j}\, g_j^{N_x}(t_k)\right\},$$

and when $K(x, y) = xy$,

$$J_i^{N_x}(t_k) = \sum_{p=1}^{i-1} \Delta x g_p^{N_x}(t_k) \left\{ \int_{x_{mid(i-p)}}^{x_{i-p+1}} \frac{x_{mid(p)} y}{y} dy \, g_{i-p}^{N_x}(t_k) + \sum_{j=i-p+1}^{N_x - 1} \int_{x_j}^{x_{j+1}} \frac{x_{mid(p)} y}{y} dy \, g_j^{N_x}(t_k) \right\},$$

which after integration gives us

$$J_i^{N_x}(t_k) = \sum_{p=1}^{i-1} \Delta x g_p^{N_x}(t_k) \left\{ .5 \Delta x \cdot x_{mid(p)} \, g_{i-p}^{N_x}(t_k) + \sum_{j=i-p+1}^{N_x - 1} x_{mid(p)} \Delta x \, g_j^{N_x}(t_k) \right\}.$$

Appendix B

Solution at $t = 0$ for $K(x, y) = xy$

For the analytical solution used in the paper when $K(x, y) = xy$, note that $f(0, x) = \frac{e^{-x}}{x}$, which is not necessarily obvious. The derivation of those initial conditions follow. From (2.23)

$$f(t, x) = e^{(-Tx)} \frac{I_1(2x\sqrt{t})}{x^2\sqrt{t}} \tag{B.1}$$

where

$$T = \begin{cases} 1 + t & \text{if } t \leq 1 \\ 2\sqrt{t} & \text{otherwise} \end{cases}$$

and we use the modified Bessel function of the first kind

$$I_1(x) = \frac{1}{\pi} \int_0^\pi e^{x \ \cos\theta} \cos\theta d\theta.$$

For this solution, $f(0, x) = \frac{e^{-x}}{x}$. Note that for $t \leq 1$

$$f(t, x) = \frac{e^{(-x-tx)} I_1(2x\sqrt{t})}{x^2\sqrt{t}}$$

with

$$I_1(2x\sqrt{t}) = \frac{1}{\pi} \int_0^\pi e^{(2x\sqrt{t}\cos\theta)} \cos\theta d\theta.$$

Now note the following:

(1) $\lim_{t\to 0} \frac{I_1(2x\sqrt{t})}{x^2\sqrt{t}} = \lim_{t\to 0} \frac{1}{\pi} \int_0^\pi \frac{e^{(2x\sqrt{t}cos\theta)} \cos\theta}{x^2\sqrt{t}} d\theta$

(2) $\mathrm{e}^{(2x\sqrt{t}\cos\theta)} = 1 + (2x\sqrt{t}\cos\theta) + \frac{(2x\sqrt{t}\cos\theta)^2}{2!} + \cdots$

therefore,

$$\begin{aligned}\lim_{t\to 0}\frac{I_1(2x\sqrt{t})}{x^2\sqrt{t}} &= \lim_{t\to 0}\frac{1}{\pi}\int_0^{\pi}\frac{\cos\theta+2x\sqrt{t}\cos^2\theta}{x^2\sqrt{t}}d\theta+\frac{1}{\pi}\int_0^{\pi}\lim_{t\to 0}\left[\frac{(2x\sqrt{t}\cos\theta)^2\cos\theta}{2!x^2\sqrt{t}}+\cdots\right]d\theta\\ &= \lim_{t\to 0}\frac{1}{\pi}\int_0^{\pi}\frac{\cos\theta}{x^2\sqrt{t}}d\theta+\lim_{t\to 0}\frac{1}{\pi}\int_0^{\pi}\frac{2\cos^2\theta}{x}d\theta+0\\ &= 0+\lim_{t\to 0}\frac{2}{\pi x}(\frac{\pi}{2})=\frac{1}{x}\end{aligned}$$

from which it follows that

$$\lim_{t\to 0}f(t,x)=\left[\lim_{t\to 0}e^{(-x-tx)}\right]\left[\lim_{t\to 0}\frac{I_1(2x\sqrt{t})}{x^2\sqrt{t}}\right]=\frac{e^{-x}}{x}.$$

Appendix C

Solution Domain choices for aggregation kernels

The theoretical $\mathcal{D}$ on which the PGSFs are defined starts at a point $\mathbf{0} \in \mathbb{R}^N$. For our purposes, the PGSFs incorporate $\left(\frac{\partial f}{\partial \gamma}\right)^2$, so when we examine the lower ends of $\mathcal{D}$, we consider the limit as $t, x \to 0^+$ of $\left(\frac{\partial f}{\partial \gamma}\right)^2$. In this appendix, we determine $\lim_{t,x \to \mathbf{0}^+} \left(\frac{\partial f}{\partial \gamma}\right)^2$ for each of the the three coagulation kernels.

For $K(x, y) \equiv \gamma$,

$$f(t, x; \gamma) = \left(\frac{2}{\gamma t}\right)^2 e^{\frac{-2x}{\gamma t}},$$

therefore

$$\frac{\partial f}{\partial \gamma} = \frac{8}{t^2 \gamma^3} e^{\frac{-2x}{\gamma t}} \left[\frac{x}{t\gamma} - 1\right].$$

Then

$$\left(\frac{\partial f}{\partial \gamma}\right)^2 = \frac{64}{t^4 \gamma^6} e^{\frac{-4x}{\gamma t}} \left[\frac{x}{t\gamma} - 1\right]^2,$$

therefore

$$\lim_{(t,x)\to(0^+,0^+)} \left(\frac{\partial f}{\partial \gamma}\right)^2 = \lim_{(t,x)\to(0,0)} \frac{64}{t^4 \gamma^6} e^{\frac{-4x}{\gamma t}} \left[\frac{x}{t\gamma} - 1\right]^2,$$

which does not exist. Choosing the path $x = 0$ demonstrates the infinite limit,

$$\begin{aligned} \lim_{(t,0)\to(0^+,0^+)} \left(\frac{\partial f}{\partial \gamma}\right)^2 &= \lim_{(t,0)\to(0^+,0^+)} \frac{64}{t^4 \gamma^6} e^{\frac{-4x}{\gamma t}} \left[\frac{x}{t\gamma} - 1\right]^2 \\ &= \lim_{(t,0)\to(0^+,0^+)} \frac{64}{t^4 \gamma^6}. \end{aligned} \tag{C.1}$$

The infinite limit in (C.1) helps guide our choice of $\underline{t} = 0.2$ for $\mathcal{D}$, which ensures our PGSFs calculations remain within computer precision.

For $K(x, y) \equiv \gamma(x + y)$, $\gamma \in \mathbb{R}_+ < \infty$, $x \in (0, \infty)$, $t \in [0, \infty)$ and as adapted from [66],

$$f(t, x; \gamma) = \frac{1}{\sqrt{2\pi}} x^{-3/2} \left(e^{-\gamma t}\right) e^{-x/\left(2e^{2\gamma t}\right)}, \tag{C.2}$$

where it naturally follows that

$$f(0,x;\gamma) = \frac{1}{\sqrt{2\pi}} x^{-3/2} e^{-x/2}.$$

As we choose $\mathcal{D}$ for the additive kernel, we again consider $\lim_{(t,0)\to(0^+,0^+)} \left(\frac{\partial f}{\partial \gamma}\right)^2$ and note

$$\left(\frac{\partial f}{\partial \gamma}\right)^2 = \frac{t^2 e^{-2\gamma t} e^{\left(-xe^{-2t}\right)}}{2\pi x^3}.$$

Then for any $t = a$, where a is constant strictly greater than zero,

$$\lim_{x\to 0^+} \left(\frac{\partial f}{\partial \gamma}\right)^2 = \lim_{x\to 0^+} \frac{a^2 e^{-2\gamma a} e^{\left(-xe^{-2a}\right)}}{2\pi x^3},$$

which is infinite. Choosing $\underline{\mathrm{x}} = 0.1$ as our minimum value ensures our PGSFs calculations remain within computer precision.

For $K(x,y) \equiv \gamma xy$, $\gamma \in \mathbb{R}_+ < \infty$, $x \in (0,\infty)$, $t \in [0,1)$ and as adapted from [66],

$$f(t,x;\gamma) = \frac{1}{\sqrt{2\pi}} x^{-5/2} e^{-(1-\gamma t)^2 x/2}, \tag{C.3}$$

where it naturally follows that

$$f(0,x;\gamma) = \frac{1}{\sqrt{2\pi}} x^{-5/2} e^{-x/2}.$$

As we choose $\mathcal{D}$ for the multiplicative kernel, we again consider $\lim_{(t,0)\to(0^+,0^+)} \left(\frac{\partial f}{\partial \gamma}\right)^2$, and note

$$\left(\frac{\partial f}{\partial \gamma}\right)^2 = \frac{t^2 e^{\left(-x(\gamma t-1)^2\right)} (\gamma t - 1)^2}{2\pi x^3}.$$

Then for any $t = a$, where $a \in (0,1)$ is a constant,

$$\lim_{x\to 0^+} \left(\frac{\partial f}{\partial \gamma}\right)^2 = \lim_{x\to 0^+} \frac{a^2 e^{\left(-x(\gamma a-1)^2\right)} (\gamma a - 1)^2}{2\pi x^3},$$

which is infinite. Choosing $\underline{\mathrm{x}} = 0.1$ as our minimum value ensures our PGSFs calculations remain within computer precision.

Appendix D

Challenges associated with x_1: where to start the grid?

At first glance, we might intuitively assume we should simply start our grid at a volume of zero, but the known solutions with which we work in this dissertation, have sharp gradients at very small x. In fact, the solution to the multiplicative kernel actually goes to infinity when $x = 0$. This can create numerical inaccuracies over the first interval from x_1 to x_2. With that said, why not just let $x_1 > 0$? To answer that question, first consider the case when we let $x_1 = 0$ on a purely uniform grid as depicted in Figure D.1 a). Then $x_2 = \Delta x$, $x_3 = 2\Delta x$, etc., and we easily establish the pattern, $x_2 + x_2 = 2\Delta x = x_3$, $x_2 + x_3 = 3\Delta x = x_4$, $\ldots$, $x_2 + x_{N_x-1} = (N_x - 1)\Delta x = x_{N_x}$. More generally, $x_j = (j-1)\Delta x$, so $x_i + x_j = (i + j - 2)\Delta x$. Conversely, when we consider the second case, one in which we keep a truly uniform grid, but set $x_1 > 0$ (as depicted in Figure D.1 b)), the "pattern" at which particles of different grid sizes x_i and x_j aggregate to form a particle of size $x_i + x_j$ is not as simple as when we set $x_1 = 0$. In this case, $x_2 = \Delta x + x_1$, $x_3 = 2\Delta x + x_1$, etc., so $x_j = (j-1)\Delta x + x_1$and $x_i + x_j = (i+j-2)\Delta x + x_1$. More importantly, we need to know into which element $x_i + x_j$ aggregate. When $x_1 = 0$, $x_i + x_j \in [x_{i+j-2}, x_{i+j-1}]$, which is the $(i+j-2)^{th}$ element. Unfortunately, when $x_1 > 0$, we have to work harder to determine in which element $x_i + x_j$ belongs. To understand why this matters, first consider a uniform grid for which $x_1 > x_{N_x}/2$. Then $x_2 + x_2 = 2\Delta x + 2x_1 > x_{N_x}$ meaning all aggregates that we consider numerically grow larger than x_{N_x} rendering our grid useless. More realistically, $x_1 \ll x_{N_x}/2$, but for small Δx, we have to compute $x_2 + x_2$ and build our pattern from there. In the first case, where $x_1 = 0$, we always have $x_2 + x_2 = x_3$ resulting in aggregation into the second element. When $x_1 > 0$, we do not have this guarantee. Algorithmically, we find the first index, i, such that $x_i \geq 2x_2$, implying $2x_2 \in [x_{i-1}, x_i]$, the $(i-1)^{th}$ element. Let $m = i - 1$, then aggregation into all intervals smaller than the m^{th} element is zero. Furthermore, aggregation into the m^{th} element includes only the interactions between particles x_2 and x_2. Then aggregation into the $(m+1)^{th}$ element involves the interactions between x_2 and x_3, and aggregation into the $(m+2)^{th}$ element involves aggregations $x_2 + x_4 = x_2 + (x_3 + \Delta x) = 2x_2 + 2\Delta x \in [x_{i+1}, x_{i+2}]$ and $x_3 + x_3 = 2(x_2 + \Delta x) \in [x_{i+1}, x_{i+2}]$, which is the $(i+1)^{th}$ element. We continue this pattern through the $(N_x - 1)^{th}$ element, where we have aggregations $x_2 + x_{N_x-1-m+1} = x_2 + [(N_x - m - 1)\Delta x + x_1] = 2x_2 + (N_x - m - 2)\Delta x \in [x_{i+(N_x-m-2)}, x_{i+(N_x-m-1)}] = [x_{N_x-1}, x_{N_x}]$, $x_3 + x_{N_x-m-1} = x_2 + \Delta x + [(N_x - m - 2)\Delta x + x_1] = 2x_2 + (N_x - m - 2)\Delta x \in [x_{N_x-1}, x_{N_x}]$, $x_4 + x_{N_x-m-2}$, etc., where $[x_{N_x-1}, x_{N_x}]$ is the $(N_x - 1)^{th}$ element.

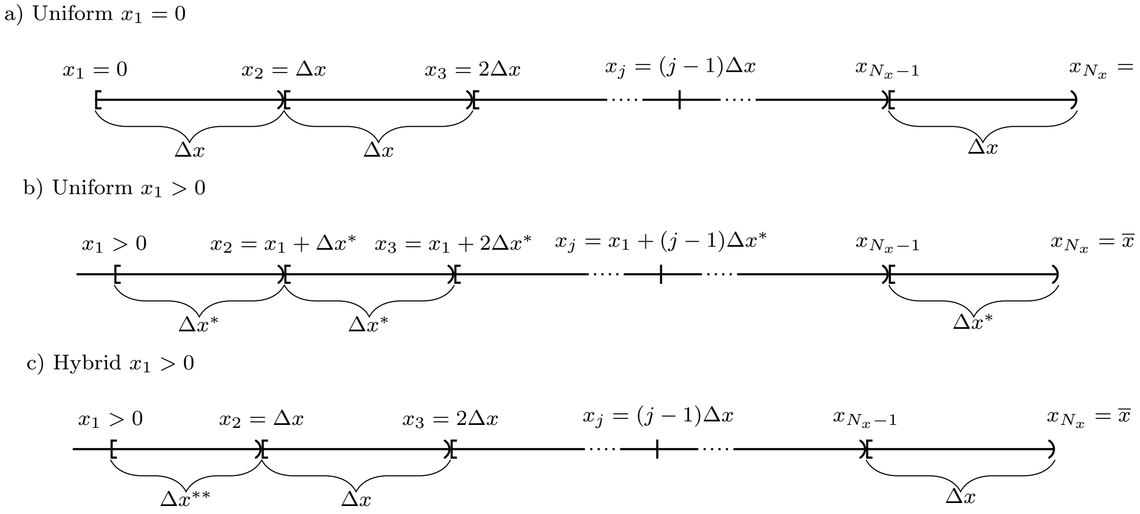

Figure D.1: Grid Possibilities. Comparison of uniform grids where $x_1 = 0$ in grid a), and $x_1 > 0$ for grids b) and c). In grids a) and c), $\Delta x = \frac{x_N}{N-1}$. In grid b), $\Delta x^* = \frac{x_N - x_1}{N-1}$, and in the hybrid grid c), $\Delta x^{**} = x_2 - x_1$.

In an attempt to simplify the numerical algorithm while avoiding the issues with $x_1 = 0$, we also generated results (not reported earlier in this dissertation) using the hybrid grid depicted in Figure D.1 c). For each case, we compare convergence and error results to the respective case's results reported in Chapter 2. Implementing the FEM and a hybrid grid as depicted in Figure D.1 c) where we manually shift x_1 to $x_1 = 0.001$ and set $K(x, y) \equiv 1$, the overall magnitude of error decreases significantly and our convergence results get slightly faster. Shifting x_1 to $x_1 = 0.75$ and setting $K(x, y) = xy$, our overall magnitude of error decreases slightly and our convergence results again get slightly faster. Implementing the FLFM and a hybrid grid with $x_1 = 0.001$ and $K(x, y) \equiv 1$, our overall magnitude of error increases slightly and our convergence results are nearly identical. Similarly, with $K(x, y) = xy$ and with $x_1 = .75$, our overall magnitude of error increases slightly and our convergence results are slightly faster.